

# A high-resolution, calibrated airborne radiometric dataset applied to the estimation of crustal heat production in the Archaean northern Pilbara Craton, Western Australia

Simon Bodorkos<sup>a,\*</sup>, Mike Sandiford<sup>a</sup>, Brian R.S. Minty<sup>b</sup>, Richard S. Blewett<sup>b</sup>

<sup>a</sup> School of Earth Sciences, University of Melbourne, Melbourne, VIC 3010, Australia

<sup>b</sup> Geoscience Australia, GPO Box 378, Canberra, ACT 2601, Australia

Received 12 March 2003; accepted 11 August 2003

## Abstract

In stable cratonised crust, the measured surface heat flow ( $q_s$ ) approximates the sum of the “deep” heat flux due to mantle convection ( $q_m$ ), and the heat flow contribution of predominantly “shallow” crust-hosted radiogenic heat production ( $q_c$ ). Archaean terrains worldwide are characterised by low and relatively uniform  $q_s$  values (30–50 mW m<sup>-2</sup>), and the common concentration of the heat-producing elements (HPEs) K, Th and U in the upper crust means that accurate estimates of HPE abundances in the major lithological units exposed are critical to the meaningful estimation of  $q_c$ . However, unit-scale geochemical datasets used for this purpose are often small and/or unevenly spatially distributed, and considerable scope exists for “average” heat production determinations that are not representative of the exposure.

This study evaluates the potential of a high-resolution (400 m flight line spacing) calibrated airborne radiometric dataset to provide reasonable area-averaged heat production estimates for major Archaean granitoid complexes within the well-exposed southern East Pilbara Granite–Greenstone Terrane (EPGGT) of Western Australia. Using the available geochemical data as ground control, we show that the overall spatial and attribute accuracy of the radiometric data is high within felsic rocks for all HPEs, with 20–40% of all site comparisons yielding geochemical and radiometric values within 5% of each other. Departures from this trend are principally attributable to: (1) K depletion of the surface layer sampled by gamma-ray spectrometry, due to the mobility of K in weathering environments, and (2) U enrichment or depletion in the surface layer reflecting disequilibrium in the <sup>238</sup>U decay chain affecting the gamma-ray response. However, both trends proved systematic and correctable at the scale of individual granitoid complexes, and we derive area-averaged heat production ( $H$ ) estimates in the range 1.5–3.0 μW m<sup>-3</sup> for the volumetrically dominant pre-2.9 Ga EPGGT granites, rising to  $H = 4.0–6.5$  μW m<sup>-3</sup> for small, late-stage (c. 2.85 Ga) plutons.

Integration of these data with independent geophysical and geochemical constraints on upper crustal structure in the EPGGT suggests that observed heat flow in the East Pilbara ( $q_s = 35–50$  mW m<sup>-2</sup>) comprises  $q_m = 10–15$  mW m<sup>-2</sup> and  $q_c = 25–40$  mW m<sup>-2</sup>, and this latter range shows considerable overlap with  $q_c$  values deduced for many Proterozoic crustal segments worldwide. This implies that HPE abundance alone does not exert primary control on the preservation of Archaean crust, and it is likely that geologic processes that concentrate HPEs in the uppermost crust play an important role in cooling and strengthening the upper lithosphere, thereby increasing its thermal and mechanical resistance to subsequent reworking.

© 2003 Elsevier B.V. All rights reserved.

**Keywords:** Archaean; Gamma-ray spectra; Granites; Heat flow; Pilbara Craton; Radioactive isotopes

\* Corresponding author. Tel.: +61-3-8344-6933; fax: +61-3-8344-7761.

E-mail address: [bodorkos@unimelb.edu.au](mailto:bodorkos@unimelb.edu.au) (S. Bodorkos).

## 1. Introduction

Most of the Earth's continents represent the products of complex and often protracted histories of crust–mantle differentiation and reworking. Prior to effective cratonisation of the crust, the intensity, style and duration of tectonic activity fundamentally depends on the thermal and mechanical properties of the lithosphere, and these properties are in turn affected by this activity, implying the operation of a profound “tectonic feedback” during continent formation (Sandiford et al., 2001). In this context, Archaean terrains with areally extensive low-grade metamorphic rocks are of particular interest as they represent lithospheric fragments that have withstood significant tectonic reactivation for the past 2.5 billion years.

Archaean cratonic nuclei worldwide are characterised by two critical geodynamic properties. Firstly, they are underlain by mantle lithosphere that is strong, chemically buoyant (e.g. Jordan, 1978, 1988; Pollack, 1986) and thick (>200–250 km; e.g. Grand and Helmberger, 1984; Boyd et al., 1985; Polet and Anderson, 1995; Simons et al., 1999; Ritsema and van Heijst, 2000; Artemieva and Mooney, 2001). Secondly, surface heat flow measurements in Archaean terrains are generally low relative to the global continental mean value of  $65 \pm 1.6 \text{ mW m}^{-2}$  (Pollack et al., 1993); a mean value of  $41 \pm 11 \text{ mW m}^{-2}$  was determined by Nyblade and Pollack (1993) from 188 measurements within Archaean cratons of North America, Europe and Africa. In view of the strongly temperature-dependent rheology of the lithosphere (e.g. Brace and Kohlstedt, 1980), both properties have important implications for the long-term mechanical strength of Archaean cratons.

However, the extent to which mantle lithosphere thickness and surface heat flow are related remains the subject of considerable debate. In tectonically stable regions, the measured heat flow represents a combination of (1) a “deep” asthenospheric mantle component (denoted  $q_m$ ) applied to the base of the conductive lithosphere, and (2) a “shallow” component (denoted  $q_c$ ) resulting from the radioactive decay of the heat-producing elements (HPEs) K, Th and U hosted by the conductive lithosphere, and concentrated in the crust. Therefore, the surface heat flow difference commonly observed between Archaean cratons and their neighbouring terrains may be explained by: (1)

diversion of asthenospheric mantle heat flux by the thick lithospheric roots developed beneath the cratons (e.g. Ballard and Pollack, 1987; Nyblade et al., 1990), (2) lower bulk concentrations of HPEs in preserved Archaean crustal segments relative to the surrounding terrains (e.g. Morgan, 1985; Lenardic, 1997), or some combination of these two factors (e.g. Nyblade and Pollack, 1993; McLennan and Taylor, 1996).

The importance of obtaining quantitative constraints on the abundance and distribution of HPEs in Archaean crust is best illustrated by considering the role of radiogenic heating in the shaping of thermal regimes in the crust and upper mantle. First-order estimates of the “deep mantle” contribution to the surface heat flow may be derived from a simple one-dimensional thermal model of the conductive lithosphere that neglects the role of radiogenic heat production. Assuming a temperature- and depth-independent bulk thermal conductivity  $k = 3.0 \text{ W m}^{-1} \text{ } ^\circ\text{C}^{-1}$  and a present-day temperature difference of  $1300 \text{ } ^\circ\text{C}$  between the Earth's surface and the base of a 250–300 km thick cratonic lithosphere, Fourier's Law yields  $q_m \sim 10\text{--}15 \text{ mW m}^{-2}$  (e.g. Jaupart and Mareschal, 1999). Values of  $q_m$  in this range are supported directly by lithosphere-scale geothermal gradients derived from thermobarometric studies of kimberlite-hosted mantle xenoliths (summarised in Rudnick and Fountain, 1995) and indirectly by constraints on bulk compositions of continental crust (and therefore  $q_c$ ) that are based on mass-balance considerations (McLennan and Taylor, 1996). The crustal heat flow contribution is then determined by difference, using  $q_s \sim 30\text{--}50 \text{ mW m}^{-2}$  as the range of typical surface heat flow values in Archaean cratons (Nyblade and Pollack, 1993), which yields  $q_c$  values in the range  $20\text{--}40 \text{ mW m}^{-2}$  and implies that at least two-thirds of the *present-day* heat flux must be attributed to predominantly crust-hosted HPEs. The importance of this result is underlined by the fact that the secular radioactive decline in radionuclide abundances since c. 2.7 Ga has halved radiogenic heat production in typical Archaean felsic crust.

It is therefore imperative that present-day HPE contents are accurately estimated in Archaean crust, and the integration of geochemistry and seismic velocity data to produce “typical” (global mean/median) compositions for various major lithotypes and crustal levels in terrains of all ages represents considerable

progress toward this objective (e.g. Rudnick and Fountain, 1995; Taylor and McLennan, 1995; Rudnick et al., 1998). Nevertheless, imposing constraints on bulk compositions at the scale of individual Archaean cratonic segments remains difficult. Firstly and in general, the volume proportions of granite and greenstone are poorly known even in “typical” Archaean crust. Secondly, only broad constraints exist regarding the proportion of continental crust extracted from the mantle during the Archaean, and the timing of such major lithospheric differentiation events is critical to compositional estimates that rely on crust–mantle mass-balance calculations (e.g. McLennan and Taylor, 1996). Thirdly, well-exposed vertical sections through Archaean crust are relatively rare (see Rudnick et al., 1998), and geochemical traverses aimed at determining HPE depth distribution patterns (e.g. Nicolaysen et al., 1981; Weaver and Tarney, 1984; Ashwal et al., 1987; Fountain et al., 1987) rarely delineate any systematic trend beyond the strong correlation between HPE content and rock type (see also Vigneresse and Cuney, 1991).

Even at the Earth’s surface, the regional estimation of radiogenic heat production may be complicated if the available geochemistry is sparse, non-representative and/or of variable analytical quality. This study evaluates the potential of an alternative approach, involving the use of a high-resolution, calibrated radiometric dataset (acquired by Geoscience Australia) to quantify the surface abundance and spatial distribution of HPEs in the East Pilbara Granite–Greenstone Terrane (EPGGT) of Western Australia. The EPGGT is uniquely suited to such an analysis, as (1) the Archaean rocks are fresh and generally well exposed, (2) the subdued topography of the region means that the spectrometric estimates are relatively accurate, and (3) excellent ground control is provided by an extensive whole-rock geochemical database (OZCHEM, courtesy of Geoscience Australia) that contains some 3840 entries within the northern Pilbara Craton.

Brief descriptions of the regional geology and the physical principles of airborne gamma-ray spectrometry are followed by an account of the acquisition and processing of the East Pilbara radiometric dataset. In the area of the southern EPGGT where the radiometric image closely resembles regional geological map patterns, Landsat Thematic Mapper (TM) imagery is used to evaluate large-scale patterns in clay, iron oxide

and vegetation development, any or all of which have the potential to modify the primary gamma-ray signature of unweathered bedrock. Positional and attribute accuracy in the radiometric datasets are assessed using OZCHEM whole-rock geochemistry, with emphasis on delineating the source(s) of systematic differences between the two datasets. The relationships observed are used to estimate the area-averaged surface K, Th and U contents of map-scale sub-units with different ages within individual granitoid complexes. These data are then integrated with pre-existing geophysical constraints on the structure of the EPGGT crust and mantle lithosphere, and used as input for 2D and 3D models of steady-state heat flow aimed at placing independent constraints on the HPE parameters derived from the radiometric data.

## 2. Geological framework of the East Pilbara Granite–Greenstone Terrane

The EPGGT (Fig. 1) preserves an episodic record of crustal growth and differentiation spanning almost one billion years, and comprises Early to Late Archaean (~3.72–2.85 Ga) granitoids and greenstones (e.g. Hickman, 1983; Gruau et al., 1987; Buick et al., 1995; Nelson, 2000) that are unconformably overlain by the post-2.78 Ga, volcanic-dominated Fortescue Group (e.g. Griffin, 1990; Arndt et al., 1991; Thorne and Trendall, 2001). It displays classic regional-scale “dome-and-keel” crustal architecture (Fig. 1), with broad (up to 120 km diameter) domal felsic plutonic complexes separated by narrow synclinal supracrustal keels dominated by mafic and ultramafic (komatiitic) volcanic rocks. The reader is referred to Van Kranendonk et al. (2002) for a recent, comprehensive synthesis of the regional geology and the role of the EPGGT in the tectonic framework of the northern Pilbara Craton.

In the EPGGT, the oldest preserved greenstones (pre-3.3 Ga) were accumulated as a series of volcanic-dominated packages each up to several kilometres in thickness, with thick basal komatiitic and tholeiitic basalt flows overlain by predominantly felsic volcanic rocks and capped by chemical sedimentary units. During this early period, felsic igneous activity in the EPGGT was strongly episodic: each major phase of andesite–rhyolite volcanism was accompanied by

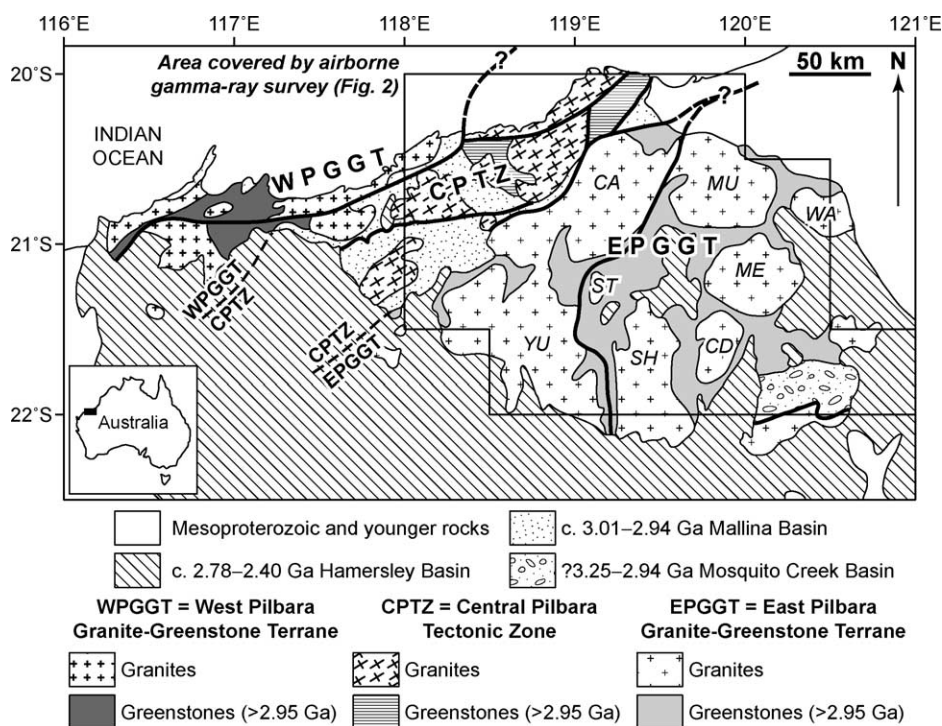


Fig. 1. Simplified geological map of the northern Pilbara Craton, showing major tectonic elements and the areal extent of the radiometric dataset. Note the regional pattern of dome-and-keel structure in the East Pilbara Granite–Greenstone Terrane (EPGGT). Abbreviations for names of granitoid complexes in the EPGGT: CA, Carlindi; CD, Corunna Downs; ME, Mount Edgar; MU, Muccan; SH, Shaw; ST, Strelley; WA, Warrawagine; YU, Yule.

granitoid plutonism, but felsic magmatic events were of relatively short duration (<10 million years) and separated by much longer periods of quiescence.

The oldest granitoid rocks of regional extent are tonalite–trondhjemite–granodiorite (TTG) suites with U–Pb SHRIMP zircon ages clustered in the interval 3.47–3.46 Ga and 3.45–3.43 Ga, respectively (e.g. Nelson, 1998), that are contemporaneous with the eruption of the felsic volcanic Duffer and Panorama Formations. These intrusions dominate exposure in the Shaw Granitoid Complex (e.g. Bickle et al., 1993; Van Kranendonk, 2000) but occur as minor components in nearly all of the EPGGT domes. The next major plutonic episode was contemporaneous with eruption of the 3.32–3.31 Ga Wyman Formation, and predominantly affected the eastern EPGGT, where granodiorite and monzogranite of this age comprises the vast volumetric majority of the Mount Edgar, Corunna Downs and Warrawagine granitoid complexes (Collins, 1993;

Barley and Pickard, 1999; Nelson, 2000, 2001; Van Kranendonk et al., 2001). Structural and stratigraphic relations in the vicinity of the Corunna Downs Granitoid Complex (Van Kranendonk et al., 2001; Bagas et al., 2002) imply that major dome-and-keel formation was initiated in the eastern EPGGT at this time (and possibly prior to the corresponding event observed in the western EPGGT; see Blewett, 2002).

Localised mafic and felsic volcanism resulted in the accumulation of the 3.25–3.23 Ga Sulphur Springs Group in the western EPGGT, and emplacement of the 3.24 Ga Strelley Granite laccolith (Fig. 1) into the greenstone sequence (Van Kranendonk, 2000 and references therein). Supracrustal rocks of the post-3.23 Ga Gorge Creek Group then covered the entire EPGGT, unconformably overlying all older rocks. Age constraints on this unit are scarce, but steeply dipping basalt and banded iron formation units that occur higher in the Gorge Creek Group sequence are



found in the cores of greenstone keel structures in the northwestern EPGGT, suggesting that deposition pre-dated the initiation of dome-and-keel formation in this area (Blewett, 2002).

Amalgamation of the western EPGGT and the Central Pilbara Tectonic Zone (CPTZ, Fig. 1) commenced at c. 2.95 Ga, and voluminous monzogranite plutonism at 2.95–2.92 Ga was accompanied by the rapid deposition of coarse clastic De Grey Group sediments into small, fault-bounded intracratonic basins formed via sinistral transpression at c. 2.94 Ga (e.g. Van Kranendonk and Collins, 1998). Within the EPGGT, a final episode of felsic magmatism at c. 2.85 Ga (Nelson, 1998) produced low-volume, highly fractionated pegmatite and leucocratic granite plutons within the Shaw, Yule and Mount Edgar granitoid complexes (Hickman, 1983; Collins, 1989; Bickle et al., 1993; Champion and Smithies, 2000).

Much of the pre-2.8 Ga Pilbara Craton is unconformably overlain by the c. 2.78 Ga basal Fortescue Group (Hickman, 1983; Arndt et al., 1991; Wingate, 1999; Thorne and Trendall, 2001). Within the EPGGT, Fortescue Group outliers preserve steeply dipping strata within pre-existing greenstone keels, implying that late-scale amplification of dome-and-keel structure locally post-dates c. 2.78 Ga Fortescue volcanism (Van Kranendonk, 2003 and references therein).

### 3. Airborne gamma-ray spectrometry: physical principles, advantages and limitations

Gamma-ray spectrometry is based on the characterisation of energetic ionising radiation emitted during the radioactive decay of unstable isotopes of potassium ( $^{40}\text{K}$ ), thorium ( $^{232}\text{Th}$ ) and uranium ( $^{235}\text{U}$  and  $^{238}\text{U}$ ), and their daughter products. During radioisotope breakdown, the emission of alpha and/or beta particles leaves the new nucleus in an excited state. Gamma-rays (which represent the radiation of this surplus energy) are characterised by two physical properties fundamental to the viability of airborne gamma-ray spectrometry as a tool for the remote sensing of terrestrial radioactivity. Firstly, each gamma-ray photon has a discrete energy that is characteristic of the source radioisotope. Secondly, gamma rays lack both mass and charge, and may pen-

etrate up to 30 cm of rock, or up to several hundred metres of air (e.g. Minty, 1997).

In terms of the quantitative estimation of area-averaged surface radiogenic heat production in a well-exposed terrane such as the EPGGT, high-resolution airborne gamma-ray spectrometry has some obvious advantages over methods of estimating the composition of the crust based on surface and/or bedrock geochemical sampling. Even if a pre-existing and relatively large geochemical compilation is available, the possibility that samples were collected for a variety of purposes other than the calculation of area-averaged composition estimates (even for first-order lithologic map units) inevitably introduces bias associated with non-uniform spatial distribution of data sites and/or non-uniform representation of lithotypes by area of exposure. An airborne survey removes all such bias.

However, the use of airborne gamma-ray spectrometric data to quantify HPE concentrations is complicated by factors that influence accuracy. Potential sources of error may be subdivided into two broad groups: (1) intractable technical shortcomings stemming from non-ideality in the physical basis of data collection and processing, and (2) obscuring of the “target” (i.e. bedrock) radiometric signature by surface processes such as physical and chemical weathering, and associated factors (including soil and clay development, and vegetation cover) that potentially vary widely across any survey area. We address the technical limitations in the following, and directly evaluate surface-related control on the East Pilbara radiometric dataset in the following section.

Of the abundant HPEs,  $^{40}\text{K}$  is the only radionuclide that emits gamma rays with a characteristic photopeak of sufficient energy (1.46 MeV) to be measured directly by conventional TI-doped NaI detector crystals. Neither  $^{232}\text{Th}$  nor  $^{238}\text{U}$  emit any gamma rays at all during the initial stage of their respective decay series. Instead, the abundance of  $^{232}\text{Th}$  is estimated using the photopeak of daughter radionuclide  $^{208}\text{Tl}$  (which is the ninth nuclide in the  $^{232}\text{Th}$  decay chain, and emits 2.61 MeV gamma rays during beta-decay to  $^{208}\text{Pb}$ ). Similarly, the abundance of  $^{238}\text{U}$  is estimated using the photopeak of daughter nuclide  $^{214}\text{Bi}$  (10th nuclide in the  $^{238}\text{U}$  decay chain, and emits 1.76 MeV gamma rays during beta-decay to  $^{214}\text{Po}$ ), and converted to

total U using the present-day isotopic abundance ratio  $^{238}\text{U}/^{235}\text{U} = 137.88$ .

Implicit in such estimations is the assumption that the decay chains between the target parent nuclides ( $^{232}\text{Th}$  and  $^{238}\text{U}$ ) and the measured daughter nuclides ( $^{208}\text{Tl}$  and  $^{214}\text{Bi}$ ) are in equilibrium within the system of interest, i.e. that decay products are neither removed nor introduced by physical or chemical processes. Once the system (which in this case is the layer within 30 cm of the Earth's surface) is disturbed, the duration of disequilibrium depends directly on the half-life of the affected radioisotope (99.9% re-equilibration is attained over a time interval approximately equal to 10 times the relevant half-life; e.g. Minty, 1997). In this respect, substantial disequilibrium is rarely encountered in the  $^{232}\text{Th}$  decay system, as all intervening nuclides (including  $^{208}\text{Tl}$ ) have extremely short half-lives (ranging from 0.145 s to 5.75 years, e.g. Ivanovich and Harmon, 1992).

Unfortunately, the  $^{238}\text{U}$  decay series has a distinctly different character, and U-series disequilibrium is one of the major sources of error in airborne gamma-ray spectrometry (Minty, 1997). Several of the unstable isotopes between  $^{238}\text{U}$  and  $^{214}\text{Bi}$  are readily fractionated by common geological, surficial and atmospheric processes, and/or have relatively long half-lives. High in the decay chain, the long-lived radioisotopes  $^{234}\text{U}$  (half-life =  $2.48 \times 10^5$  years),  $^{230}\text{Th}$  (half-life =  $7.52 \times 10^4$  years) and  $^{226}\text{Ra}$  (half-life =  $1.6 \times 10^3$  years) exhibit varying degrees of solubility and mobility in surface environments, particularly during clay formation and changes in oxidation state but also during uptake into plant tissue (e.g. Minty, 1997; Dickson and Scott, 1997). Fractionation of these isotopes is thus common, and re-equilibration of the decay series is very slow (from tens of thousands to millions of years).

However, one of the most serious sources of disequilibrium in the  $^{238}\text{U}$  decay series is related to the mobility of gaseous  $^{222}\text{Rn}$  (produced by alpha decay of  $^{226}\text{Ra}$ ). Although  $^{222}\text{Rn}$  has a half-life of only a few days, its escape into the atmosphere from surface cracks and fissures in soils and rocks is facilitated by climate-controlled changes in temperature and pressure, which have a "pumping" effect (see Minty, 1997). Local disequilibrium problems are exacerbated by the tendency of its daughter products (including

$^{214}\text{Bi}$ ) to attach themselves to airborne aerosols and dust particles, resulting in a radionuclide distribution largely controlled by air movements and wind patterns (Minty, 1997). This phenomenon complicates data acquisition and processing, as the ground  $^{214}\text{Bi}$  signature may be obscured by a significant atmospheric  $^{214}\text{Bi}$  component (comprising up to 20–50% of the signal measured in the U window; Minty et al., 1997) that is unrelated to the surface geology within the field of view of the gamma-ray detector.

#### 4. Acquisition and processing of the Pilbara dataset

Radiometric data were collected over much of the Pilbara Craton during the course of airborne geophysical surveys conducted by the Australian Geological Survey Organisation (AGSO, now Geoscience Australia) in 1996 (see Richardson, 1997 for operational details). Survey lines were flown east–west at 400 m spacing, and were tied by north–south lines at 4 km spacing. Gamma-ray spectra were sampled at 1 s intervals, using an Exploranium gamma-ray spectrometer (incorporating two DET1024 crystal detectors with a total volume of 33.56 litres). Over the energy range 0–3 MeV, 256 channels of data were collected and the following five energy windows were monitored constantly: total count (0.40–3.00 MeV), potassium (1.35–1.57 MeV), uranium (1.63–1.89 MeV), thorium (2.42–2.82 MeV) and cosmic radiation (3.00–6.00 MeV).

Following detector deadtime correction and energy calibration, aircraft, cosmic and atmospheric  $^{222}\text{Rn}$  background were removed, and the gamma-ray spectra summed to the energy windows described above. The window count rates were then stripped (channel interaction correction) and corrected for deviations in the aircraft height from the nominal flying height of 80 m. The corrected elemental count rates were converted to ground concentrations of K (in wt.%) and equivalent Th and U (eTh and eU, respectively, both in ppm). Residual levelling errors were removed using cross-over tie levelling and micro-levelling. The fully corrected radioelement data were then gridded to a cell size of 80 m using a minimum curvature algorithm. Richardson (1997) gives full details of the processing procedures.

## 5. A high-resolution radiometric dataset for the East Pilbara Granite–Greenstone Terrane

Fig. 2a is a red–green–blue (RGB) image portraying the calibrated Pilbara radiometric dataset, with the red, green and blue channels corresponding to

K, equivalent Th and equivalent U, respectively (see also Wellman, 1998b; Wellman, 1999; Blewett et al., 2000). As airborne gamma-ray spectrometry can only provide information about HPE concentrations within a few tens of centimetres of the Earth's surface, any attempt to use the data to estimate bedrock HPE contents

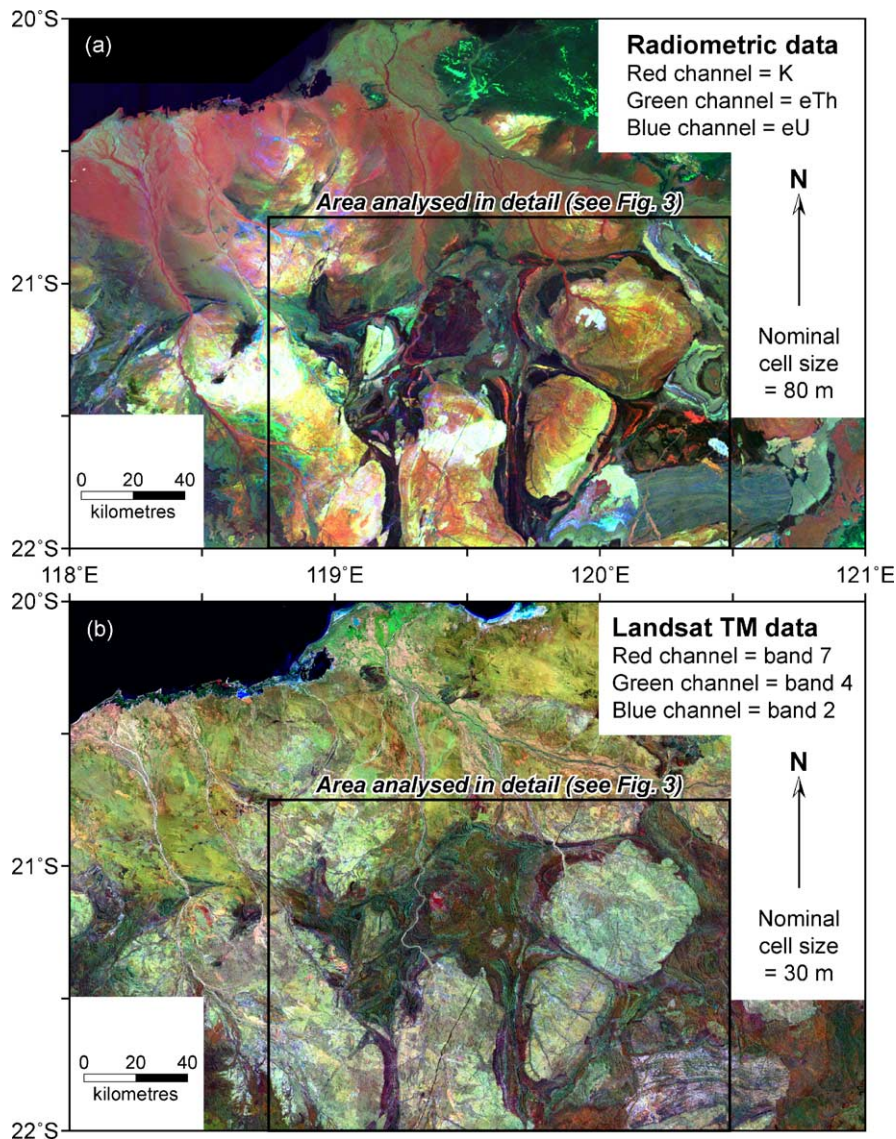


Fig. 2. (a) Red–green–blue (RGB) image showing Geoscience Australia's calibrated radiometric dataset for the northern Pilbara Craton (see Fig. 1 for location). Potassium (K), equivalent thorium (eTh) and equivalent uranium (eU) are shown in the red, green and blue channels, respectively. (b) RGB image derived from Landsat Thematic Mapper (TM) data for the same area. The red, green and blue channels correspond to band 7 (infra-red; wavelength 2.08–2.35  $\mu\text{m}$ ), band 4 (near infra-red; wavelength 0.76–0.90  $\mu\text{m}$ ) and band 2 (visible green; wavelength 0.52–0.60  $\mu\text{m}$ ), respectively.

must account for the potential of weathering-related surface processes to obscure the underlying geology. In this regard, the radiometric data are most obviously useful in areas where bedrock is well exposed, especially if locally occurring, unconsolidated colluvium and/or regolith material is substantially in situ and has undergone minimal chemical modification during weathering.

One independent means of assessing the effect of large-scale, surface-related processes on the measured gamma-ray spectrum is provided by Landsat TM images of the same area (see Glikson, 1998), and the two images in Fig. 2 show excellent first-order agreement at terrane-scale. Floodplains in the northern part of the Pilbara Craton are characterised by the development of an extensive and relatively thick layer of transported colluvial material (and associated smearing and homogenisation of the measured gamma-ray spectra; Fig. 2a), and a very similar pattern is evident in the Landsat image (Fig. 2b). In contrast, exposure in the southern part of the EPGGT is excellent (especially in the framed area within Fig. 2), the boundaries between the granitoid complexes and their flanking greenstone belts are sharply defined on both images, and agree very well with regional geological map patterns (Fig. 1; see also Hickman and Lipple, 1978).

However, much of the finer geological detail is more clearly represented in the radiometric data than in the Landsat image shown here (see also Glikson, 1998). For example, gamma-ray spectrometry effectively delineates relatively thin (but HPE-rich) felsic volcanic units within the greenstone keel separating the Shaw and Corunna Downs Granitoid Complexes. Similarly, stark lithologic contrasts between tholeiitic basalt and interbedded quartz-rich sedimentary rocks in the Fortescue Group outlier southeast of the Mount Edgar Granitoid Complex are faithfully reproduced by the radiometric data. Within the granitoid complexes, sharp contacts between map-scale sub-units are clearly defined by the gamma-ray spectrometry, particularly within the Shaw and Mount Edgar batholiths. Many of these second-order compositional variations are relatively muted in the Landsat images (Glikson, 1998), suggesting that the observed contrasts in the gamma-ray response reflect real differences in bedrock HPE concentrations between lithological units (rather than large-scale, systematic

enrichment or depletion of HPEs by surface processes such as clay eluviation and/or pedogenesis).

The good qualitative correlation between the first-order geological units, the gamma-ray data and the Landsat image within the framed area of Fig. 2 means that this region is suitable for more detailed quantitative analysis of the radiometric dataset. Fig. 3a is a greyscale image of this spatial subset, depicting present-day volumetric heat production (in  $\mu\text{W m}^{-3}$ ) calculated from the calibrated K, Th and U data, assuming a constant density  $\rho = 2700 \text{ kg m}^{-3}$  throughout. Fig. 3b shows first-order sub-units within the granitoid complexes and greenstone belts, corresponding to felsic and mafic magmatic events of various ages. Most of these sub-units are easily distinguished in Fig. 3a.

These sub-units can be used to assess the role of local surface weathering processes (distinguishable via Landsat imagery) in modifying the measured gamma-ray response within the granitoid complexes. Within each sub-unit, the extent of internal variation in each of the HPEs (Fig. 4a–c) is compared to the corresponding internal variation of Landsat band ratios typically used to highlight the development of clay, iron oxides and vegetation (Fig. 4d–f). In all cases, each cell value is expressed in terms of its difference from the area-averaged mean value of the enclosing sub-unit, measured in standard deviations (Fig. 4).

All granitoid sub-units display internal variations in HPE concentrations (especially K; see Fig. 4a) that are substantially greater than that evident in the Landsat spectral ratios stretched over the same scale. Furthermore, there is little spatial correspondence between HPE variation and Landsat spectral ratio variations over much of the imaged area (see also Glikson, 1998; Wellman, 1998b). In general, the best correlation is observed between areas of Th depletion (Fig. 4b) and areas of Fe oxide enrichment (Fig. 4e) in the southern and eastern parts of the image. These two images also reveal the greatest detail in the drainage patterns, which suggests that Th and Fe oxide concentrations are sensitive to processes involving physical transportation of weathered material. Importantly, the Landsat band ratio delineating clay (Fig. 4d) displays poor spatial correlation with both K and U variations (Fig. 4a and c) throughout, implying that the role of large-scale clay eluviation and/or selective leaching of HPEs does not significantly complicate the



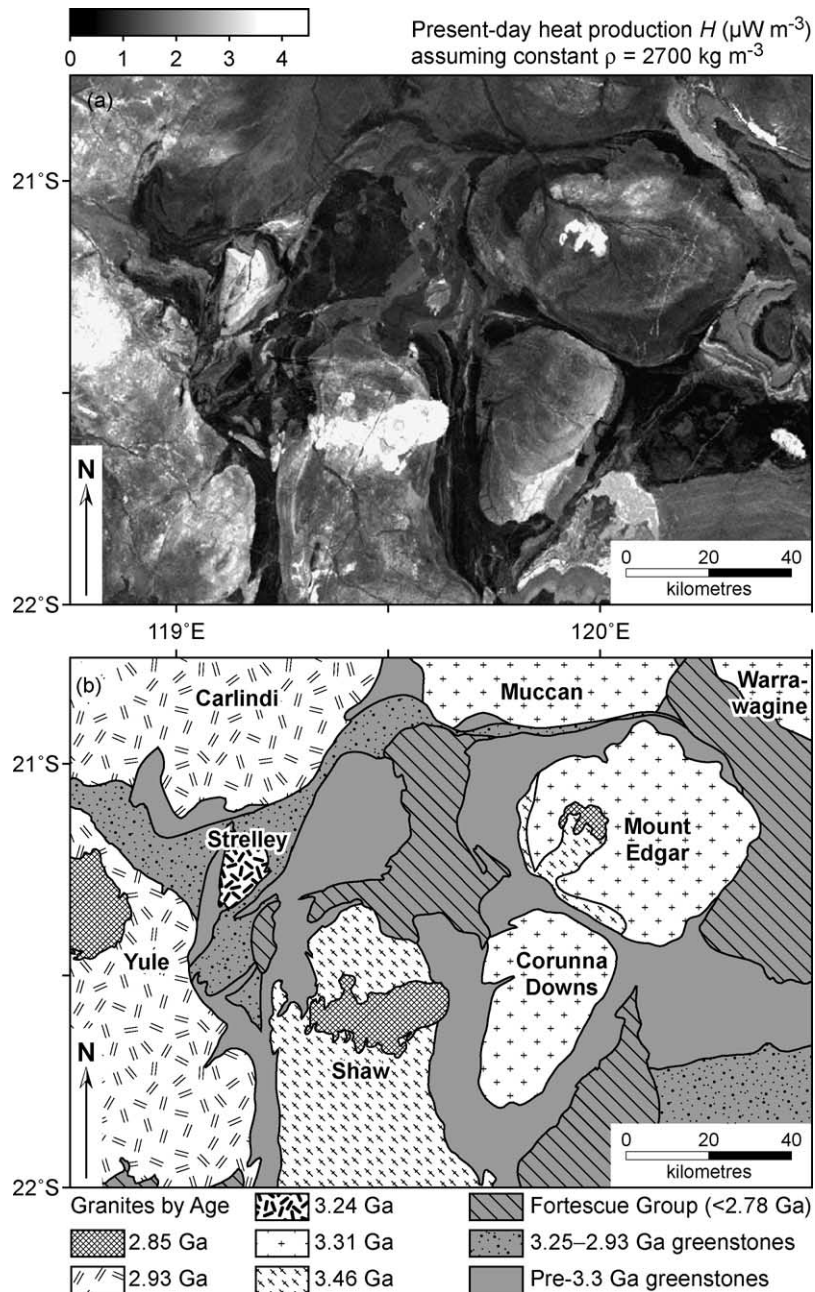


Fig. 3. (a) Greyscale image depicting present-day heat production for the area enclosed by the frame in Fig. 2, calculated from the calibrated radiometric dataset. The following isotopic proportions were assumed:  $^{40}\text{K}/\text{K} = 1.28 \times 10^{-4}$ ,  $^{232}\text{Th}/\text{Th} = 1.00$ ,  $^{235}\text{U}/\text{U} = 7.2 \times 10^{-3}$  and  $^{238}\text{U}/\text{U} = 0.9927$ , with heat release per unit mass:  $^{40}\text{K} = 27.9 \mu\text{W kg}^{-1}$ ,  $^{232}\text{Th} = 26.9 \mu\text{W kg}^{-1}$ ,  $^{235}\text{U} = 569.0 \mu\text{W kg}^{-1}$ ,  $^{238}\text{U} = 93.7 \mu\text{W kg}^{-1}$  (values from Turcotte and Schubert, 1982). Note that a uniform density  $\rho = 2700 \text{ kg m}^{-3}$  was assumed over the entire area. (b) Simplified geologic map of the southern EPGGT, showing the first-order lithological sub-units used to interrogate the radiometric dataset. Granitoid complexes are divided into units with characteristic U–Pb SHRIMP zircon ages (using data summarised by Van Kranendonk et al., 2002) with boundaries defined by regional map patterns (e.g. Hickman and Lipple, 1978) that coincide with zones of high contrast in Fig. 3a.

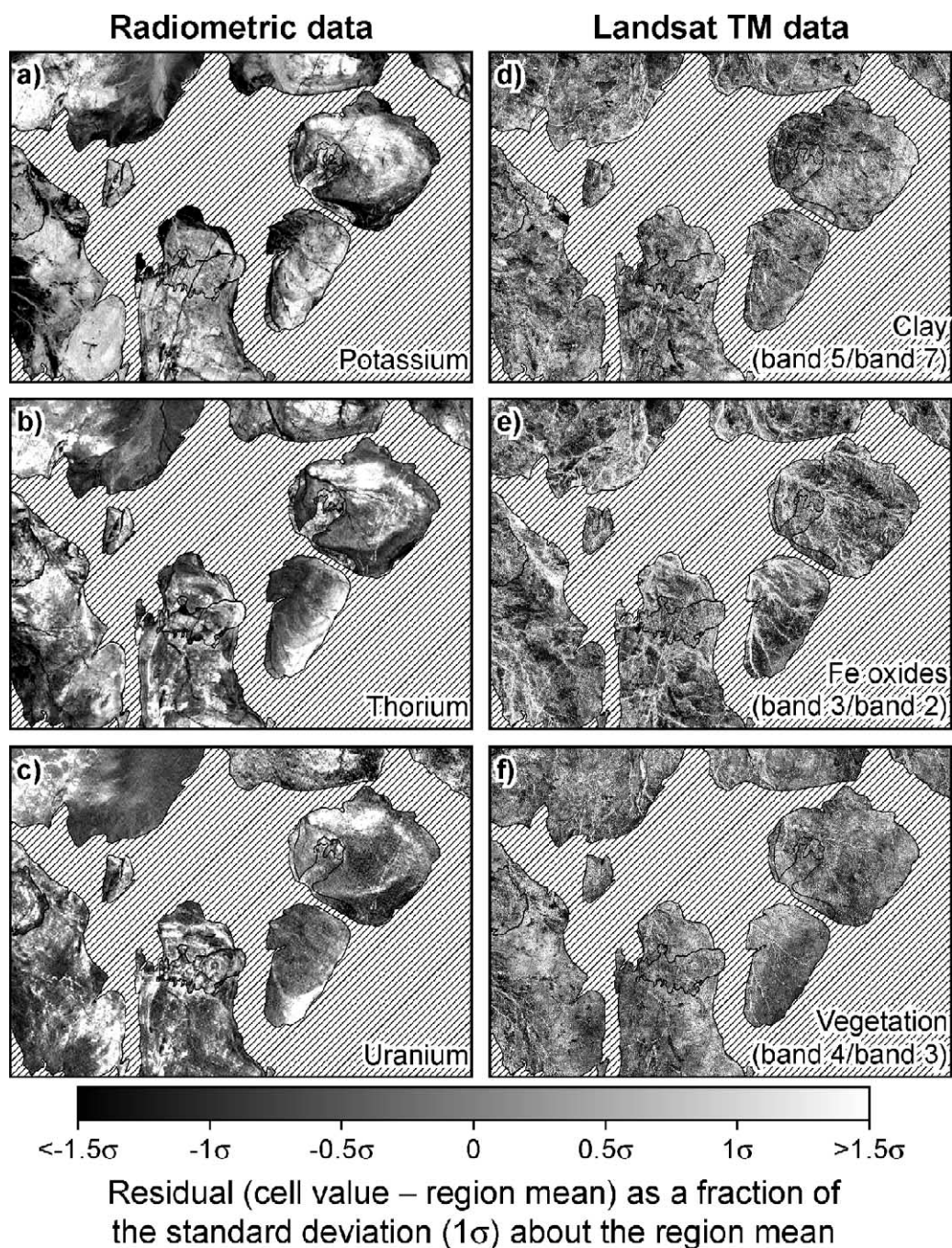


Fig. 4. Images illustrating the extent of internal variation in gamma-ray response (a–c) and Landsat band ratios (d–f) within each of the granitic sub-units defined in Fig. 3b. For each sub-unit, the difference between each individual cell and the mean value for the sub-unit is expressed as a fraction of the standard deviation for that sub-unit (see Table 2 for HPE values). The greyscale range for each sub-unit is centred on the mean and stretched over three standard deviations.



relationship between regolith and bedrock HPE concentrations in the granitoids (cf. Dickson and Scott, 1997; Wilford et al., 1997). In addition, the Landsat band ratio delineating vegetation displays little internal variation (and negligible correlation with HPE distributions), consistent with the results of previous studies which suggest that gamma-ray response is little affected by vegetation in arid parts of Australia (e.g. Bierwirth, 1996; Wilford et al., 1997).

This combination of results implies that the observed variations in gamma-ray response between granitoid sub-units reflect real differences in bedrock geochemistry, and that surface processes have not significantly obscured the primary radiometric signatures (Glikson, 1998).

## 6. A method for comparing the OZCHEM geochemical data to the radiometric image

In this section, we assess attribute and positional accuracy in the calibrated radiometric dataset using whole-rock geochemical analyses from Geoscience Australia's OZCHEM compilation, which is the most complete and up-to-date database available for the Pilbara region, and contains 2206 entries within the area of Fig. 3. A frequency histogram of SiO<sub>2</sub> contents for this OZCHEM subset (Fig. 5) displays a bimodal distribution, with peaks at 49–52 and 68–72 wt.% separated by lower frequencies over the range 55–62 wt.%. On this basis, the database was subdivided into two major groupings: mafic rocks (SiO<sub>2</sub> = 38–60 wt.%) and felsic rocks (SiO<sub>2</sub> = 60–80 wt.%). Spatial comparisons of the geochemical and radiometric K, Th, and U values within the area of Fig. 3 were carried out separately for each grouping using the following procedure.

OZCHEM samples for which the relevant HPE was not analysed or not detected were discarded, and the remaining data were sorted by sample site latitude and longitude. Each group of samples sharing identical geographic co-ordinates was then combined into a single value equal to the arithmetic mean of the subset at that site. Each sample in this reduced OZCHEM dataset was then compared with a 5 × 5 matrix of cell values from the radiometric dataset, centred on the cell in closest geographic proximity. From this matrix, the cell closest in value to the OZCHEM sample value

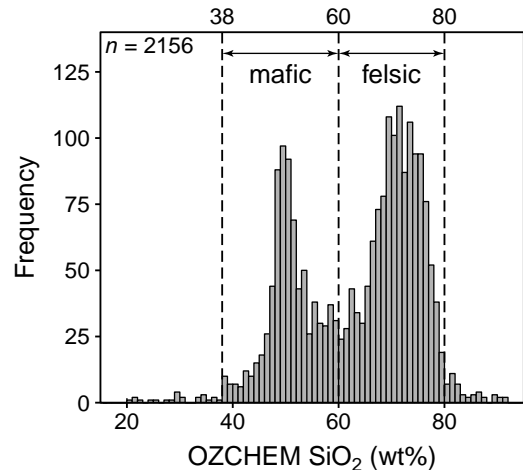


Fig. 5. Frequency histogram showing OZCHEM whole-rock geochemical data within the area enclosed by Fig. 3 by SiO<sub>2</sub> content (50 additional analyses have no SiO<sub>2</sub> data or lie outside the histogram range). The pronounced bimodal distribution defined by the peaks at 49–52 and 68–72 wt.% (and low frequencies over the interval 55–62 wt.%) allows simple subdivision of the dataset into felsic (SiO<sub>2</sub> > 60 wt.%) and mafic (SiO<sub>2</sub> < 60 wt.%) rocks.

(hereafter referred to as the “best cell” value) was extracted and used for data comparison.

This approach has two major advantages. It minimises spurious HPE mismatches arising from relatively minor spatial discrepancies between the geochemical and radiometric datasets. This is especially important with respect to geochemical samples collected near the contact(s) of two (or more) units with significantly different HPE contents, and the use of a centred 5 × 5 matrix means that errors in the reported geographic co-ordinates of OZCHEM sample sites of up to 200 m in any direction are tolerated (for a nominal cell size of 80 m in the radiometric image). In addition, the approach provides partial compensation for the fact that the “field of view” for individual cells in the radiometric dataset is likely to substantially exceed the grid cell size (see Fig. 12; Minty, 1997). This spatial averaging inherent in the radiometric data means that the range of HPE values for a given unit will often be narrower than the range defined by the corresponding geochemical dataset (Wellman, 1998b), due to the fact that the gamma-ray response of low-volume sub-units with anomalous HPE contents will usually be swamped by the response of rocks with more “representative”

HPE contents that dominate the spectrometer field of view. In contrast, anomalous sub-units are often over-represented in geochemical datasets not collected specifically for the purpose of area-averaged HPE estimates (cf. Kukkonen and Lahtinen, 2001).

Nevertheless, the comparative approach used here has three important limitations. Firstly, it is necessary to assume that each OZCHEM sample is geochemically representative of the dominant rock type at that site, and that the combination of multiple geochemical samples from the same site into an arithmetic mean is sensible for the purpose of their comparison with the radiometric data.

Secondly, the quality of the OZCHEM data compilation is variable with respect to Th and U determinations, in terms of both the analytical precision (up to  $\pm 10$  ppm for Th and  $\pm 2$  ppm for U in some cases) and the detection limits (as high as 10 ppm Th and 2 ppm U). Such variations primarily reflect the evolution of trace-element measurement techniques over time: fortunately, the vast majority of the OZCHEM data are characterised by Th and U analyses with implied precisions of 0.1–0.5 ppm and detection limits lower than 1 ppm. While it is possible that such analytical limitations may introduce systematic bias into the estimation of HPE concentrations in mafic rocks (especially with respect to U), they are less likely to be important in the comparison of radiometric and geochemical HPE determinations in East Pilbara granitoids, which are typified by relatively high Th and U contents.

Thirdly, it is critical to recall that the conversion of gamma-ray data from counts-per-second to equivalent HPE concentrations makes *no* assumption about the density of the surface layer, which is an important factor in view of the low-density soils commonly developed over granitic rocks (cf. Dickson and Scott, 1997). Consequently, variations between radiometric and geochemical HPE determinations reflect only *preferential* enrichment or depletion of the relevant HPE in the soil profile, and do not take into account any mass wasting and/or density change accompanying pedogenesis.

## 7. Results of the comparison between the OZCHEM data and the radiometric image

K, Th and U comparisons between the OZCHEM data and the radiometric image were carried out on a sample-by-sample basis for both of the major SiO<sub>2</sub> groupings defined in the previous section (see Fig. 5), and the results are summarised in Table 1. For convenience, we express the comparison for each OZCHEM sample in terms of the ratio  $\xi$ , defined as:

$$\xi_i = \frac{\text{OZCHEM sample value}}{\text{radiometric "best cell" value}}$$

where  $i$  = K, Th or U. Fig. 6 shows the OZCHEM sample sites used for HPE comparisons in the mafic (Fig. 6a–c) and felsic (Fig. 6d–f) SiO<sub>2</sub> groupings, with

Table 1

Sample-by-sample spatial comparison of K, Th and U values derived from the geochemical and radiometric datasets, for felsic and mafic rock types

Rock group and element	$n^a$	Geochemical data <sup>b</sup>		Radiometric data <sup>c</sup>		Ratio $\xi^d$	
		Median	Mean $\pm 1\sigma$	Median	Mean $\pm 1\sigma$	Median	Mean $\pm 1\sigma$
Felsic rocks (60–80 wt.% SiO <sub>2</sub> )							
K (wt.%)	1225	2.73	2.9 $\pm$ 1.6	1.84	1.8 $\pm$ 0.6	1.42	1.6 $\pm$ 1.6
Th (ppm)	1013	11.80	15.5 $\pm$ 10.5	9.81	11.5 $\pm$ 6.3	1.09	1.4 $\pm$ 1.0
U (ppm)	977	2.30	3.2 $\pm$ 3.0	2.85	3.2 $\pm$ 1.5	0.87	0.9 $\pm$ 0.6
Mafic rocks (38–60 wt.% SiO <sub>2</sub> )							
K (wt.%)	472	0.51	0.9 $\pm$ 1.0	0.67	0.8 $\pm$ 0.6	0.96	0.9 $\pm$ 0.6
Th (ppm)	366	5.20	5.4 $\pm$ 4.1	6.34	5.9 $\pm$ 3.4	0.99	0.9 $\pm$ 0.4
U (ppm)	329	1.67	1.8 $\pm$ 3.6	2.69	2.7 $\pm$ 0.8	0.57	0.7 $\pm$ 1.5

<sup>a</sup>  $n$  = number of geographically unique OZCHEM samples with the relevant HPE concentration above the analytical detection limit.

<sup>b</sup> Data from Geoscience Australia's OZCHEM database.

<sup>c</sup> Based on "best cell" values (see text for definition).

<sup>d</sup>  $\xi$  = OZCHEM value/"best cell" value, calculated for each OZCHEM sample.



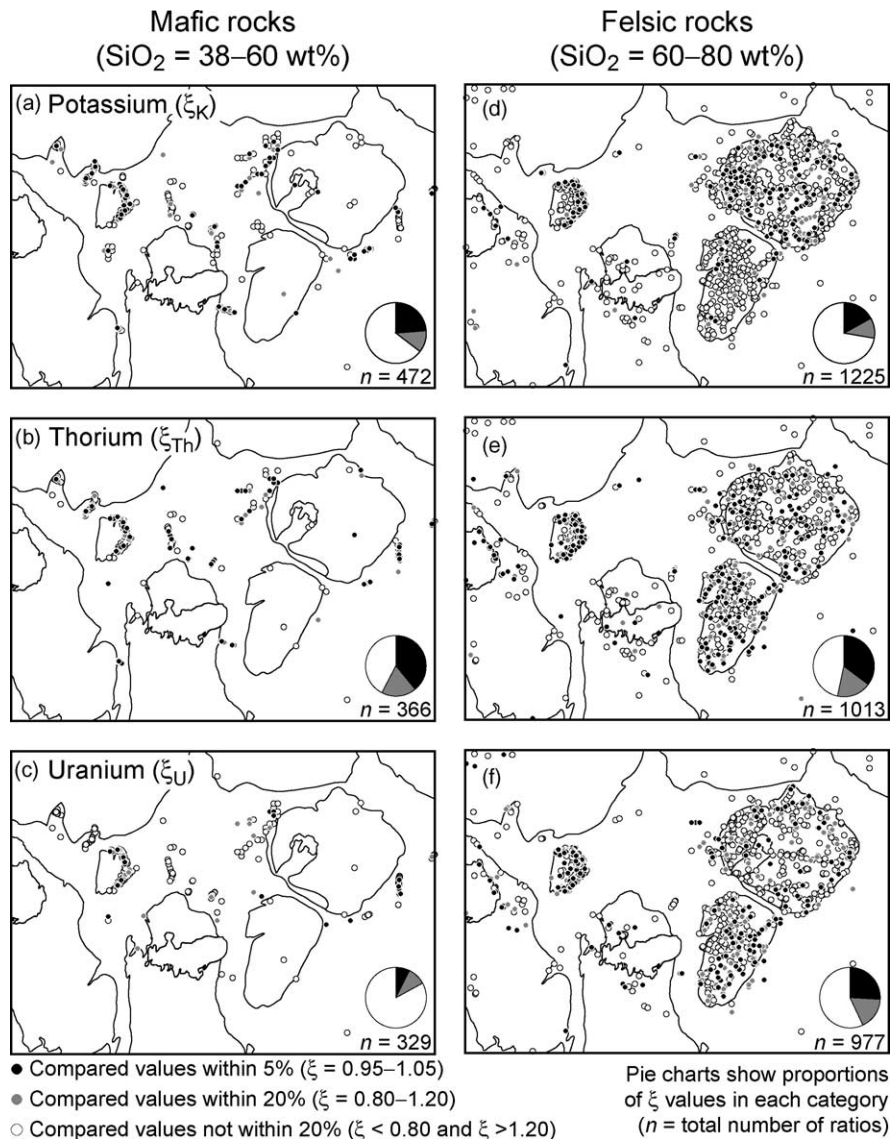


Fig. 6. Locations of OZCHEM geochemical data points for the mafic and felsic subdivisions defined in Fig. 5, for K (a and d), Th (b and e) and U (c and f). Each site is colour-coded according to the agreement between the OZCHEM value and the corresponding “best cell” value from the radiometric image (i.e. its  $\xi$  value), and the pie charts illustrate the proportion of analyses falling into each category of  $\xi$  ranges.

each site colour-coded according to the degree of correlation between the OZCHEM value and the radiometric “best cell” value at that locality.

The spatial distribution of OZCHEM sites is profoundly non-uniform for both SiO<sub>2</sub> groupings (Fig. 6). Mafic sample sites are strongly concentrated in the greenstone belts east of the Strelley Granite and also

west of the Mount Edgar Granitoid Complex, and felsic samples are predominantly situated within the Strelley, Mount Edgar and Corunna Downs granitoid complexes (see also Fig. 1). This clustering of sample sites means that “full spectrum” analysis of  $\xi$  values by SiO<sub>2</sub> content must be undertaken with caution, as it may not be appropriate to extrapolate local patterns

of  $\xi$  values in areas of high OZCHEM sample density to areas of the radiometric image with poor geochemical coverage, if the local  $\xi$  patterns are not representative of other parts of the image. An example of this potential problem is provided by  $\xi_K$  values in felsic rocks within the Corunna Downs Granitoid Complex, which comprise only 20% of the total felsic dataset ( $n = 1225$ , Fig. 6a) but account for approximately 40% of the  $\xi_K$  values within the imaged area that lie outside the range 0.80–1.20 (Fig. 6). In order to assist in the identification of such features in the data,  $\xi$  values from the dominant Mount Edgar and Corunna Downs subsets are distinguished from the rest of the felsic dataset in the following treatment.

Fig. 7 comprises frequency histograms of  $\xi_K$ ,  $\xi_{Th}$  and  $\xi_U$  for the mafic and felsic  $SiO_2$  groupings, with frequencies normalised to percentages to facilitate direct comparison of peak heights.  $\xi_K$  and  $\xi_{Th}$  spectra are characterised by pronounced frequency peaks at  $\xi = 0.95$ –1.05 in both mafic and felsic rocks (Fig. 7a and b), and a similar distribution is evident in  $\xi_U$  for the felsic rocks (Fig. 7c). These relationships imply that overall agreement between the OZCHEM value and the “best cell” radiometric value in the well-exposed southern EPGGT is excellent (within 5%) in many cases. The consistent clustering of peaks at  $\xi = 1$  suggests that: (1) gamma-ray spectrometer performance was consistent when bedrock exposure within the field of view of the detector was sufficient to appear as an infinite source of radiation (see Minty, 1997), and (2) the gamma-ray data were not significantly degraded during processing and calibration.

Interestingly, all three HPEs display different (and mostly asymmetric) frequency distributions about  $\xi = 1$  (Fig. 7), which may indicate that local surface processes influence each HPE in a different way. We examine the behaviour of K, Th and U separately in the following.

### 7.1. Potassium

Overall, 15–20% of  $\xi_K$  values lie in the range 0.95–1.05 for both the mafic and felsic rocks (Fig. 7a); however, the distribution of the outliers is dramatically different. In the mafic rocks, the data are clustered at  $\xi_K < 0.5$ , whereas the felsic data are symmetrically distributed about a weak local maximum at  $\xi_K \sim 1.6$  (Fig. 7a).

These trends are chiefly due to a combination of the mobile behaviour of K in weathering environments, and the strongly bimodal  $SiO_2$  (and  $K_2O$ ) distribution of the predominantly igneous EPGGT rocks (see Fig. 5). In terms of the K “budget” of the surface layer produced by weathering processes, felsic rocks almost always represent K sources, and mafic rocks usually represent K sinks. Consequently, nearly any process that acts to redistribute K within the surface layer will result in K depletion of soil developed above felsic rocks, and K enrichment in soil overlying mafic rocks. Within the EPGGT, this redistribution is commonly aided by topography: greenstone belts typically represent topographic highs, and the shedding of their depleted soils into low-lying granitoid-dominated areas has the effect of diluting the relatively K-rich granite soil developed in situ (see also Dickson and Scott, 1997). Within the mafic rocks, the distribution of  $\xi_K$  values implies that enrichment of the surface layer is more common than depletion relative to bedrock, possibly due to the redistribution of K-rich soils developed above felsic volcanic units within the greenstone sequences.

At a smaller scale, local variations in  $\xi_K$  are evident between granitoid complexes. While the distribution of Mount Edgar  $\xi_K$  values is broadly representative of the overall spectrum, the frequencies of  $\xi_K$  values from the Corunna Downs Granitoid Complex (which comprises over 15% of the total dataset) are very low in the range  $\xi_K = 0.0$ –1.2, and very high in the range  $\xi_K = 1.2$ –2.0 (Fig. 7a). These trends imply that K depletion of the Corunna Downs surface layer relative to bedrock is more pronounced than in soils developed over felsic rocks elsewhere within the area of Fig. 3, and such efficient leaching of K from the surface layer may be linked to the high density of drainage networks in the Corunna Downs Granitoid Complex relative to others in the region (Fig. 2).

### 7.2. Thorium

Geochemical and radiometric Th determinations display the best agreement of all the HPEs, with  $\xi_{Th} = 0.95$ –1.05 for 40% of samples in both the mafic and felsic rock groupings (Fig. 7b). In each case, the distribution is similar to that observed for  $\xi_K$ : the felsic  $\xi_{Th}$  histogram shows a weak secondary maximum at  $\xi_{Th} = 1.1$ –1.2 (with the Mount Edgar

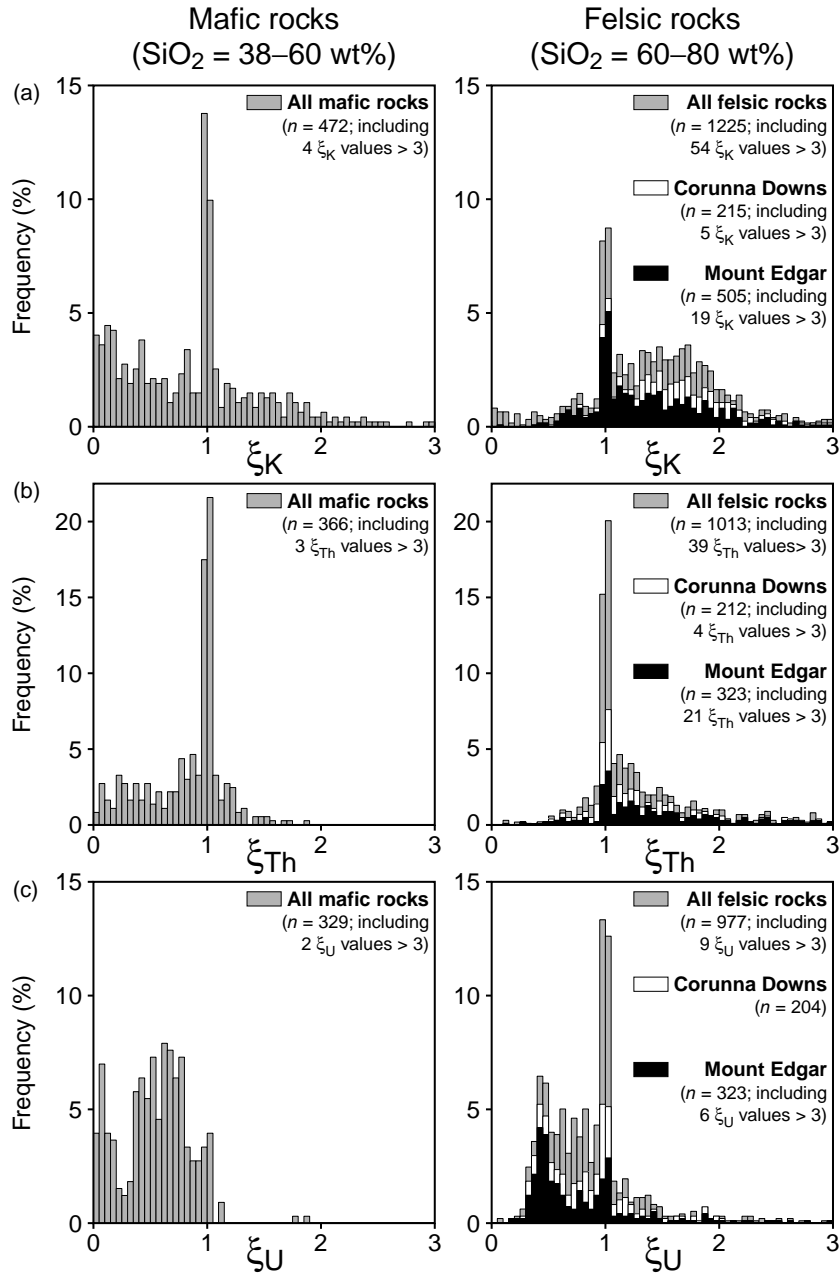


Fig. 7. Frequency histograms for the mafic and felsic subdivisions defined in Fig. 5, showing the results of an sample-by-sample comparison of each value in the OZCHEM database with the corresponding “best cell” value from the radiometric image ( $\xi$  = OZCHEM value/“best cell” value) for (a) K, (b) Th and (c) U. Within felsic rocks, the disproportionately large number of analyses from the Mount Edgar and Corunna Downs Granitoid Complexes have been distinguished from all other analyses, to emphasise the potential effect of localised  $\xi$  variations on the appearance of the “full spectrum” frequency histograms. All histograms (except  $\xi_U$  in mafic rocks) show pronounced modes at  $\xi = 0.95$ – $1.05$ .

and Corunna Downs Granitoid Complexes both being representative of the overall trend) and outliers in the mafic  $\xi_{\text{Th}}$  spectrum lie almost exclusively in the range  $\xi_{\text{Th}} = 0.1\text{--}0.9$  (Fig. 7b).

The fact that  $\xi_{\text{Th}} \sim 1$  for much of the data reflects two important properties of Th that renders it amenable to measurement via gamma-ray spectrometry. Firstly, as discussed earlier, the absence of long-lived radionuclides in the  $^{232}\text{Th}$  decay chain means that secular equilibrium is rarely disturbed (Minty, 1997). Secondly, Th is immobile (relative to K) in hydrothermal and oxidising alteration environments dominated by chemical weathering processes (e.g. Wellman, 1998a), so the surface-layer homogenisation effects (i.e. mafic  $\xi < 1$ , felsic  $\xi > 1$ ) evident in the  $\xi_{\text{K}}$  spectra are substantially muted in the  $\xi_{\text{Th}}$  data. It is therefore likely that the observed variation in  $\xi_{\text{Th}}$  values is mainly attributable to the physical homogenisation of the surface layer.

### 7.3. Uranium

The use of our comparative approach to reconcile geochemical U values with those obtained via airborne gamma-ray spectrometry presents a number of difficulties. In the mafic rocks (Fig. 7c), the  $\xi_{\text{U}}$  spectrum lacks the frequency peak at  $\xi \sim 1$  that is evident in all other spectra in Fig. 7, and most values are scattered throughout the range  $\xi_{\text{U}} = 0.4\text{--}0.7$ . In the felsic rocks, 25% of  $\xi_{\text{U}}$  values lie in the range 0.95–1.05 (Fig. 7c), but many of the outliers are concentrated around a secondary maximum at  $\xi_{\text{U}} = 0.5\text{--}0.7$ . This is primarily due to the strong over-representation of data from the Mount Edgar Granitoid Complex in this part of the spectrum (Fig. 7c).

A significant obstacle unique to the assessment of U relates to the low U abundances of most crustal materials, and the potential for relatively low-quality geochemical U determinations stemming from the associated decrease in signal-to-noise ratio. These problems preclude meaningful comparison of radiometric and geochemical data in the assessment of U concentrations in the EPGGT mafic rocks (Fig. 7c), and complicate analysis of the  $\xi_{\text{U}}$  spectrum in the felsic rocks (especially in the Mount Edgar Granitoid Complex, where fractional uncertainties associated with many of the older, low-precision OZCHEM analyses are of the order of 50–100%). Fortunately, most of

the OZCHEM U data from felsic rocks outside the Mount Edgar Granitoid Complex are more precise, and this is reflected by a clustering of  $\xi_{\text{U}}$  values in the range 0.75–1.05 for rocks with U contents significantly higher than the analytical detection limit (Fig. 7c).

Additional factors complicating the assessment of U are related to the physical basis of airborne gamma-ray spectrometric data collection (described in Section 3). Perturbation of secular disequilibrium in the  $^{238}\text{U}$  decay chain is facilitated by the ease with which U is fractionated in weathering environments (e.g. Minty, 1997), and the disparate geochemical behaviour of U isotopes with respect to unstable daughter radionuclides such as  $^{226}\text{Ra}$  (e.g. Dickson and Scott, 1997). In this context, the localised development of a relatively U-rich surface layer over the Mount Edgar Granitoid Complex may partially explain its atypical  $\xi_{\text{U}}$  spectrum (Fig. 7c). This explanation is consistent with the results of a soil U– $^{226}\text{Ra}$  disequilibrium study by Dickson (1995), which suggest that U-enriched soils are more widespread than  $^{226}\text{Ra}$ -enriched soils in Australia.

## 8. Estimation of area-averaged heat production in the East Pilbara granitoid complexes

Table 2 presents the median and mean HPE contents for each sub-unit of the granitoid complexes defined in Fig. 3b, calculated using (1) the OZCHEM database for each pluton, and (2) the radiometric data (see Fig. 2a). The median and mean values of  $\xi_{\text{K}}$ ,  $\xi_{\text{Th}}$  and  $\xi_{\text{U}}$  were also determined for each sub-unit, in order to assess the relationships between geochemical and radiometric HPE determinations at the scale of individual plutons. Such data are important as pluton-scale  $\xi$  trends are invariably swamped by the large volume of combined data used to construct the “full spectrum”  $\xi$  histograms in Fig. 7.

One disadvantage of this pluton-by-pluton comparison is that some of the sub-units defined in Fig. 3 (such as the Muccan and Warrawagine granitoid complexes; Table 2) are virtually unrepresented in the OZCHEM database, and so there is little scope for comparison of the two datasets at this scale. However, we believe that our approach is vindicated by the relatively large range in mean and median  $\xi$  values observed within sub-units with better OZCHEM coverage. Overall,  $\xi_{\text{Th}}$



Table 2

Comparison of average K, Th and U estimates derived from the geochemical and radiometric datasets

Granitoid complex <sup>a</sup> by age component		<i>n</i> <sup>b</sup>	Geochemical data <sup>c</sup>		Radiometric data <sup>d</sup>		Ratio $\xi^e$	
			Median	Mean $\pm 1\sigma$	Median	Mean $\pm 1\sigma$	Median	Mean $\pm 1\sigma$
Carlindi (by area: 100.0% = 2.93 Ga)								
2.93 Ga	K	20	2.77	2.6 $\pm$ 2.1	1.54	1.7 $\pm$ 0.7	1.36	1.3 $\pm$ 0.6
	Th	18	12.70	12.7 $\pm$ 11.1	7.79	8.9 $\pm$ 3.7	1.03	1.2 $\pm$ 0.8
	U	17	4.20	3.6 $\pm$ 2.9	2.97	3.4 $\pm$ 1.2	1.00	0.9 $\pm$ 0.7
Corunna Downs (by area: 100.0% = 3.31 Ga)								
3.31 Ga	K	223	3.75	3.7 $\pm$ 1.2	2.12	2.1 $\pm$ 0.4	1.64	1.7 $\pm$ 0.5
	Th	220	11.55	13.5 $\pm$ 7.6	10.20	12.0 $\pm$ 5.8	1.05	1.2 $\pm$ 0.6
	U	212	2.05	2.5 $\pm$ 1.5	2.78	3.0 $\pm$ 0.9	0.92	0.9 $\pm$ 0.4
Mount Edgar (by area: 86.1% = 3.31 Ga, 11.3% = 3.46 Ga, 2.6% = 2.85 Ga)								
2.85 Ga	K	11	4.72	4.7 $\pm$ 0.3	2.47	2.4 $\pm$ 0.3	1.72	1.7 $\pm$ 0.1
	Th	14	34.00	31.3 $\pm$ 12.8	23.99	23.5 $\pm$ 6.5	1.27	1.2 $\pm$ 0.3
	U	14	11.00	9.3 $\pm$ 5.1	7.46	7.5 $\pm$ 1.9	1.11	1.0 $\pm$ 0.5
3.31 Ga	K	467	2.40	2.7 $\pm$ 1.4	1.72	1.8 $\pm$ 0.5	1.32	1.5 $\pm$ 0.8
	Th	299	10.00	16.7 $\pm$ 11.6	7.57	8.5 $\pm$ 3.5	1.35	1.7 $\pm$ 1.1
	U	295	1.00	2.4 $\pm$ 2.7	2.42	2.5 $\pm$ 0.7	0.64	0.9 $\pm$ 0.7
3.46 Ga	K	58	1.96	2.4 $\pm$ 1.1	1.52	1.5 $\pm$ 0.3	1.16	1.4 $\pm$ 0.5
	Th	32	13.00	15.0 $\pm$ 7.5	6.97	7.1 $\pm$ 1.7	1.48	1.6 $\pm$ 0.7
	U	28	1.00	2.3 $\pm$ 3.3	2.60	2.7 $\pm$ 0.5	0.47	0.7 $\pm$ 0.7
Muccan (by area: 100.0% = 3.31 Ga)								
3.31 Ga	K	4	2.78	2.3 $\pm$ 1.7	1.49	1.5 $\pm$ 0.4	1.59	1.7 $\pm$ 1.4
	Th	4	15.80	13.7 $\pm$ 9.5	6.47	6.8 $\pm$ 1.8	2.09	2.0 $\pm$ 1.4
	U	4	2.50	2.8 $\pm$ 1.9	2.40	2.4 $\pm$ 0.4	1.06	1.2 $\pm$ 0.7
Shaw (by area: 84.1% = 3.46 Ga, 15.9% = 2.85 Ga)								
2.85 Ga	K	12	4.65	4.6 $\pm$ 0.5	2.81	2.8 $\pm$ 0.3	1.59	1.6 $\pm$ 0.2
	Th	11	45.00	45.4 $\pm$ 8.1	27.44	28.1 $\pm$ 9.4	1.25	1.4 $\pm$ 0.3
	U	3	19.00	17.4 $\pm$ 3.0	6.98	7.2 $\pm$ 1.9	1.76	1.8 $\pm$ 0.3
3.46 Ga	K	30	3.94	3.7 $\pm$ 1.4	2.23	2.2 $\pm$ 0.5	1.65	1.6 $\pm$ 0.5
	Th	27	21.40	24.6 $\pm$ 14.4	9.84	10.7 $\pm$ 4.0	1.87	2.1 $\pm$ 1.3
	U	19	2.50	2.6 $\pm$ 1.2	3.18	3.4 $\pm$ 0.9	0.80	0.8 $\pm$ 0.3
Strelley (by area: 100.0% = 3.24 Ga)								
3.24 Ga	K	59	4.29	3.7 $\pm$ 1.2	2.33	2.2 $\pm$ 0.4	1.65	1.5 $\pm$ 0.4
	Th	58	24.45	24.4 $\pm$ 9.6	20.80	21.0 $\pm$ 6.2	1.01	1.0 $\pm$ 0.3
	U	57	6.10	6.4 $\pm$ 2.6	4.88	5.0 $\pm$ 1.4	1.02	1.1 $\pm$ 0.4
Warrawagine (by area: 100.0% = 3.31 Ga)								
3.31 Ga	K	2	3.63	3.6 $\pm$ 0.6	1.47	1.5 $\pm$ 0.4	1.78	1.8 $\pm$ 0.1
	Th	2	13.15	13.4 $\pm$ 3.1	7.87	8.2 $\pm$ 2.1	1.59	1.6 $\pm$ 0.3
	U	2	2.40	2.4 $\pm$ 2.5	2.62	2.7 $\pm$ 0.4	0.81	0.8 $\pm$ 0.8
Yule (by area: 90.1% = 2.93 Ga, 9.9% = 2.85 Ga)								
2.85 Ga	K	10	3.95	3.8 $\pm$ 1.4	2.92	2.8 $\pm$ 0.4	1.40	1.4 $\pm$ 0.4
	Th	10	29.45	31.1 $\pm$ 11.5	28.35	28.9 $\pm$ 6.7	1.00	1.2 $\pm$ 0.3
	U	10	4.45	7.8 $\pm$ 7.5	6.51	6.9 $\pm$ 2.1	1.00	1.1 $\pm$ 0.6
2.93 Ga	K	25	3.92	3.7 $\pm$ 1.6	2.35	2.2 $\pm$ 0.7	1.61	1.5 $\pm$ 0.5
	Th	25	21.60	22.8 $\pm$ 13.9	12.20	12.9 $\pm$ 4.8	1.24	1.4 $\pm$ 0.6
	U	24	3.95	5.6 $\pm$ 5.8	3.49	3.8 $\pm$ 1.2	0.99	1.3 $\pm$ 1.4

<sup>a</sup> Age components within each of the granitoid complexes are defined in Fig. 3b.<sup>b</sup> *n* = number of geographically distinct OZCHEM samples within each region for which the relevant HPE concentration is above the analytical detection limit.<sup>c</sup> K in wt.%, Th and U in ppm.<sup>d</sup> All values area-averaged using the regions defined in Fig. 3b (K in wt.%, eTh and eU in ppm).<sup>e</sup>  $\xi$  = OZCHEM value/"best cell" value, calculated for each OZCHEM sample.

and  $\xi_U$  display the most variation (Table 2), with median and mean  $\xi_{Th}$  values, respectively, ranging from 1.01 and  $1.0 \pm 0.3$  (Strelley) up to 1.87 and  $2.1 \pm 1.3$  (Shaw). Median and mean  $\xi_U$  values are in the range 0.47 and  $0.7 \pm 0.7$  (Mount Edgar) up to 1.02 and  $1.1 \pm 0.4$  (Strelley), respectively.  $\xi_K$  values are much more uniform between and within sub-units (Table 2), with median and mean  $\xi_K$  values, respectively, ranging from 1.36 and  $1.3 \pm 0.6$  (Carlindi) up to 1.72 and  $1.7 \pm 0.1$  (Mount Edgar).

Nearly all of the granitic sub-units are characterised by mean and median  $\xi > 1$  for all HPEs, and this is principally due to the widespread operation of weathering processes that variably deplete the surface layer of K, Th and U (see Section 7). This surface-layer HPE depletion is accurately reflected by a simple compar-

ison (by sub-unit) of the mean volumetric heat production calculated from the OZCHEM data with that estimated from the radiometric data. The first two sets of columns in Table 3 summarise these results: all sub-units yield a mean heat production calculated from the gamma-ray data that is 10–50% lower than that determined from OZCHEM (although the scatter in the geochemical data is substantial, even within individual plutons).

Based on the relatively uniform nature of the discrepancy between the two datasets, we apply a simple, “pluton-by-pluton” manipulation of the radiometric data that is aimed at providing first-order compensation for relatively minor HPE depletion (or, more rarely, enrichment) in the surface layer at sub-unit scale during weathering. The approach is

Table 3

Comparison of average volumetric heat production estimates derived from the geochemical and radiometric datasets, and the effect of  $\xi$ -multiplication

Granitoid complex by age component	$n^a$	Heat production, $H$ (in $\mu\text{W m}^{-3}$ , assuming $\rho = 2700 \text{ kg m}^{-3}$ ) from					
		Geochemical data		Radiometric data <sup>b</sup>		$\xi$ -multiplied radiometrics <sup>c</sup>	
		Median	Mean $\pm 1\sigma$	Median	Mean $\pm 1\sigma$	Median	Mean $\pm 1\sigma$
Carlindi							
2.93 Ga	16	3.16	$2.3 \pm 1.6$	1.36	$1.5 \pm 0.5$	1.39	$1.6 \pm 0.6$
Corunna Downs							
3.31 Ga	212	1.72	$1.9 \pm 0.9$	1.46	$1.7 \pm 0.6$	1.54	$1.8 \pm 0.7$
Mount Edgar							
2.85 Ga	11	6.43	$6.1 \pm 1.0$	3.72	$3.7 \pm 0.8$	4.18	$4.1 \pm 0.9$
3.31 Ga	209	1.60	$2.2 \pm 1.5$	1.19	$1.3 \pm 0.4$	1.47	$1.6 \pm 0.5$
3.46 Ga	17	1.39	$1.9 \pm 1.6$	1.19	$1.2 \pm 0.2$	1.27	$1.3 \pm 0.3$
Muccan							
3.31 Ga	4	2.03	$1.9 \pm 1.3$	1.10	$1.1 \pm 0.2$	1.65	$1.7 \pm 0.3$
Shaw							
2.85 Ga	3	8.64	$8.3 \pm 1.0$	3.91	$3.9 \pm 1.0$	6.15	$6.2 \pm 1.5$
3.46 Ga	19	2.33	$2.6 \pm 1.3$	1.57	$1.7 \pm 0.5$	2.22	$2.4 \pm 0.7$
Strelley							
3.24 Ga	57	3.85	$3.8 \pm 1.2$	2.80	$2.9 \pm 0.8$	2.96	$3.0 \pm 0.8$
Warrawagine							
3.31 Ga	2	1.88	$1.9 \pm 1.0$	1.26	$1.3 \pm 0.2$	1.47	$1.5 \pm 0.3$
Yule							
2.85 Ga	10	3.44	$4.6 \pm 2.4$	3.78	$3.9 \pm 0.9$	4.20	$4.4 \pm 1.0$
2.93 Ga	24	2.91	$3.5 \pm 2.4$	1.85	$1.9 \pm 0.6$	2.47	$2.6 \pm 0.8$

<sup>a</sup>  $n$  = number of geographically distinct OZCHEM samples with K, Th and U concentrations that are *all* above analytical detection limits.

<sup>b</sup> All values area-averaged using the regions defined in Fig. 3b.

<sup>c</sup> Based on cell-by-cell multiplication of the K, eTh and eU values for each cell by the (constant) mean  $\xi_K$ ,  $\xi_{Th}$  and  $\xi_U$  values of the enclosing region (see Table 2 for  $\xi$  values).

straightforward: it simply utilises the mean  $\xi_K$ ,  $\xi_{Th}$  and  $\xi_U$  values for each sub-unit (see Table 2) as constant multiplicative factors for each cell value within the area enclosed by that sub-unit. For example, the relevant manipulation of the radiometric data within the Carlindi Granitoid Complex (Fig. 3) is achieved by multiplying all K cell values by 1.3, all equivalent Th (eTh) values by 1.2, and all equivalent U (eU) values by 0.9 ( $\xi$  values from Table 2). These “ $\xi$ -multiplied” data may then be used to recalculate area-averaged heat production statistics, and the results are summarised in the third set of columns in Table 3.

The net effect of this manipulation is to bring the heat production estimates from the radiometric data much closer to those derived from the geochemistry (Table 3). Differences between the mean heat production values obtained from the  $\xi$ -multiplied data and those derived from the OZCHEM data are less than 30%, and the former values commonly lie well within one standard deviation of the latter (Table 3). The  $\xi$ -multiplication process therefore has two major advantages with respect to the estimation of area-averaged heat production in the bedrock. Firstly, it provides a first-order reconciliation of the radiometric and geochemical datasets at locations where ground control data exist. Secondly, the “natural” advantages of airborne gamma-ray spectrometry outlined in Section 3 are preserved (i.e. the spectrum of data collected is less sensitive to outliers than a comparatively sparse geochemical sampling program, and the associated smoothing of small-scale internal variation decreases the standard deviation associated with the mean  $\xi$ -multiplied values at sub-unit scale; see Table 3).

The heat production values estimated from the  $\xi$ -multiplied values for each unit also highlight consistent spatial and geochemical trends within individual granitoid complexes, at the scale of the first-order subdivision used in Fig. 3b. Within the eastern EPGGT, pre-3.3 Ga rocks with characteristic  $\xi$ -multiplied  $H = 1.5\text{--}2.5 \mu\text{W m}^{-3}$  dominate exposure, and similar  $H$  values were derived for the volumetrically dominant sub-units of Carlindi and Yule in the western EPGGT (Table 3). In addition, all of the multi-component granitoid complexes exhibit remarkably uniform and substantial HPE enrichment, often culminating in the intrusion of relatively small, late plutons with  $\xi$ -multiplied  $H$  values ranging from  $4.1 \pm 0.9 \mu\text{W m}^{-3}$

(Mount Edgar) and  $4.4 \pm 1.0 \mu\text{W m}^{-3}$  (Yule) up to  $6.2 \pm 1.5 \mu\text{W m}^{-3}$  (Shaw). In each case, the c. 2.85 Ga plutons are characterised by HPE contents up to 150% higher than those of the host granitoids (Table 3).

## 9. Data integration and estimation of the EPGGT crustal heat production budget

In this section we test the first-order validity of the surface heat production values calculated for the EPGGT granites, by integrating them with pre-existing geophysical and geochemical data constraining the first-order geometry and structure of the crust at depth. The aim is to develop simple thermal models for the EPGGT lithosphere that can be evaluated in terms of the constraints imposed by surface heat flow measurements. In the upper crust, modelling of gravity and magnetic data suggests that most of the East Pilbara granitoid complexes resemble steep- to vertical-sided cylindrical bodies that extend to depths of 10–14 km (Wellman, 2000), and seismic refraction models show a small but distinct velocity increase (from  $\sim 6.2$  to  $\sim 6.4 \text{ km s}^{-1}$ ) at 13–15 km depth (Drummond, 1983). Seismic and gravity data suggest that the lower crust comprises relatively low-velocity material of similar density to the upper crustal greenstone sequences (possibly felsic granulite; Drummond, 1988). At the base of the crust, the Moho is defined by a large seismic velocity discontinuity (from  $\sim 6.8$  to  $>8.0 \text{ km s}^{-1}$ ) that typically occurs over an interval of 5–10 km at 28–35 km depth in the northern Pilbara Craton (Drummond, 1988). Deep seismic tomography studies suggest that the thickness of the Pilbara Craton lithosphere is of the order of 250 km (e.g. Simons et al., 1999; Artemieva and Mooney, 2001).

### 9.1. Model geometries and thermal parameters

Using the above constraints on the structure of the EPGGT crust and lithosphere, we briefly consider steady-state thermal models for two simple geometric configurations. In the two-dimensional model, we use a cross section comprising 60% granite, 40% greenstone by area in the uppermost 14 km of the crust (proportions based on surface exposure in the

## (a) Model geometry

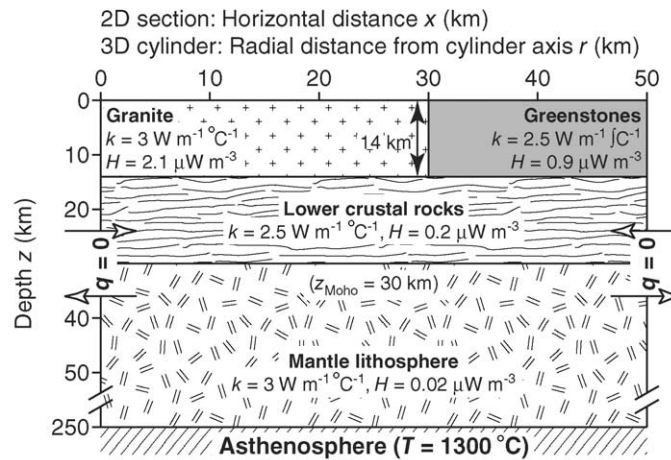
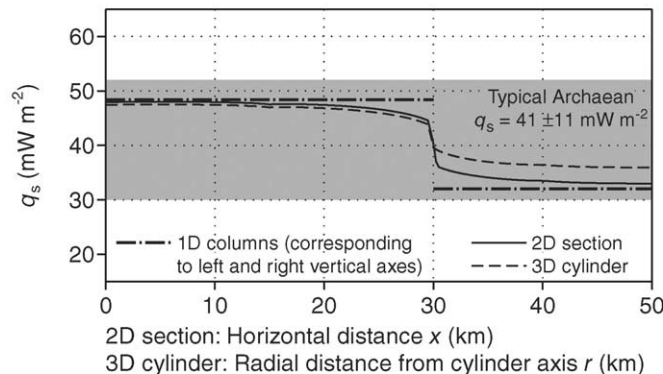
(b) Surface heat flow ( $q_s$ )

Fig. 8. (a) Geometry of the model lithosphere used to assess the surface heat flow field generated by the observed crustal structure. The 2D model assumes that the uppermost 14 km of the East Pilbara crust comprises 60% granite, 40% greenstone by volume, and the 3D model represents a simple extension of the 2D system into a cylindrical geometry by rotation about the vertical axis  $x = 0$  (which transforms the lithologic volume proportions in the upper crust to 36% granite, 64% greenstone). Zero net heat transfer ( $q = 0$ ) across the left and right edges of the 2D system (corresponding to the vertical axis and outer surface of the 3D cylinder) simulates conditions at the midpoint of a granite “dome” and a greenstone “keel”, respectively. (b) Lateral variation in surface heat flow for the 2D and 3D systems, computed by solving the steady-state heat equation for the geometries described in (a). The 1D vertical surface heat fluxes highlight the extent of lateral homogenisation in the 2D and 3D heat flow fields due to compositional heterogeneity of the upper crust. Both models yield heat flow values across the profile that lie well within the typical Archaean  $q_s$  range (Nyblade and Pollack, 1993).

EPGGT, see Fig. 2), overlying a 16 km thick, homogeneous lower crust and a 220 km thick mantle lithosphere (see Fig. 8). We then extend this model to a three-dimensional cylindrical geometry, with the cylinder defined by rotation of the 2D cross-section described above about the vertical axis  $x = 0$  (Fig. 8). Note that this transformation changes the volume proportions of granite and greenstone in the system,

with the inner cylinder of granite comprising only 36 vol.% of the uppermost 14 km of the crust.

The thermal parameters used are summarised in Fig. 8a (note that for simplicity, thermal conductivity and volumetric heat production are assumed depth- and temperature-independent within each lithospheric component). For granite and greenstone, typical thermal conductivity values were taken from



compilations of laboratory data (e.g. Haenel et al., 1988; Beardsmore and Cull, 2001), and the granite heat production value is representative of the  $\xi$ -multiplied data for areally extensive components of the East Pilbara granitoid complexes (Table 3). As discussed in Section 7.3, the radiometric data cannot be meaningfully used to estimate mean greenstone heat production, so we use the OZCHEM subset with  $\text{SiO}_2 = 38\text{--}60\text{ wt.}\%$  as a proxy for the dominant lithologies. The median HPE values ( $K = 0.5\text{ wt.}\%$ ,  $\text{Th} = 5.2\text{ ppm}$  and  $\text{U} = 1.7\text{ ppm}$ ; see Table 1) yield  $H = 0.9\text{ }\mu\text{W m}^{-3}$ , which is slightly higher than that typical of the most common mafic greenstone compositions. However, the discrepancy provides partial compensation for the fact that the OZCHEM  $\text{SiO}_2$  range used for this calculation does not account for the contribution of HPE-rich felsic volcanic rocks (with  $\text{SiO}_2 > 60\text{ wt.}\%$ ) within the greenstone stratigraphy.

Little lower crustal material is exposed in the EPGGT, so Drummond (1988) used a combination of seismic velocity and gravity data to infer that amphibolite- to granulite-facies gneisses dominate at depth. It is likely that such rocks contain significant proportions of hornblende and feldspar, and a bulk average  $k = 2.5\text{ W m}^{-1}\text{ }^\circ\text{C}^{-1}$  (e.g. Beardsmore and Cull, 2001) is appropriate to the relatively shallow depth range (14–30 km; Drummond, 1983) inferred for the lower crustal layer. In the absence of any direct constraint from the EPGGT, we assume  $H = 0.2\text{ }\mu\text{W m}^{-3}$ , based on a global mean  $H = 0.18\text{ }\mu\text{W m}^{-3}$  for Archaean lower crust derived by Rudnick and Fountain (1995).

We use  $k = 3\text{ W m}^{-1}\text{ }^\circ\text{C}^{-1}$  for the mantle lithosphere, which broadly reflects the temperature-dependent increase in thermal conductivity (from the lower crustal value) expected at depth. The bulk average  $H = 0.02\text{ }\mu\text{W m}^{-3}$  for the mantle lithosphere is based on the results of thermal models optimised for the Archaean Slave Craton by Russell et al. (2001), which are supported by geotherms synthesised from kimberlite-hosted xenolith thermobarometry by Rudnick et al. (1998).

## 9.2. Results

Results of the steady-state 2D and 3D thermal models are expressed in terms of the expected surface heat field (Fig. 8b), which provides a useful basis of

comparison with extant surface heat flow ( $q_s$ ) measurements. Unfortunately, only four heat flow determinations exist for the greater Pilbara Craton, all of which are confined to the Hamersley Basin south of the EPGGT (Cull, 1982, 1991). However, all four values lie in the range  $q_s = 39\text{--}46\text{ mW m}^{-2}$ , well within the global “typical” Archaean range ( $q_s = 41 \pm 11\text{ mW m}^{-2}$ ) defined by Nyblade and Pollack (1993).

In our 2D and 3D models, the “envelope” of possible heat flow values is defined by the special 1D “granite-only” and “greenstone only” cases corresponding to the left- and right-hand vertical axes of Fig. 8a ( $q_s \sim 48\text{ mW m}^{-2}$  and  $q_s \sim 32\text{ mW m}^{-2}$ , respectively; Fig. 8b). Between these two extremes, the 2D and 3D  $q_s$  profiles display significant lateral homogenisation, primarily due to relatively shallow-level horizontal heat transfer stemming from the substantial heat production contrast at the granite–greenstone interface. This effect is accentuated in the 3D cylinder by the radial nature of horizontal heat conduction (Fig. 8b).

The results suggest that, subject to the assumptions and limitations inherent in our simple models, an EPGGT lithospheric heat production budget dominated by upper crustal granite with a mean  $H$  value derived from the  $\xi$ -multiplied data in Table 3 yields an equilibrium thermal structure consistent with the constraints imposed by surface heat flow. Most importantly, the deconvolution of  $q_s$  predicted by our models (i.e. the respective overall contributions of “deep mantle” ( $q_m$ ) and “shallow crust” ( $q_c$ ) heat flow components) is not particularly sensitive to reasonable variations in the thermal and structural parameters used. In general, asthenospheric mantle heat flux  $q_m \sim 10\text{--}15\text{ mW m}^{-2}$  for sensible thermal conductivity models and lithospheric thicknesses (see also Russell et al., 2001), and by difference, the contribution of radiogenic heat sources in the conductive EPGGT lithosphere  $q_c \sim 20\text{--}40\text{ mW m}^{-2}$ . With the exception of the anomalously high heat-producing Precambrian lithosphere of northern Australia (e.g. Sandiford and Hand, 1998; Sandiford and McLaren, 2002), the range of  $q_c$  values calculated for the EPGGT is not significantly different to those estimated for many Proterozoic terrains worldwide (see Artemieva and Mooney, 2001 for a summary), and the implications of this important result are discussed below.

### 9.3. Implications for the thermal evolution of Archaean lithosphere

The similarity between the range of  $q_c$  values inferred for the EPGGT and those postulated for typical Proterozoic terrains is significant, as it implies that the absolute abundance of HPEs in the crust does not always exert primary control on the preservation of ancient lithosphere (cf. Morgan, 1985). However, the fact that  $q_c$  comprises two-thirds of the present-day surface heat flow in the EPGGT suggests that crustal HPE contents play a pivotal role in shaping the geotherm, especially as radioactive decay has reduced typical mid-Archaean crustal heat production rates by 50–60% since c. 3.0 Ga. It is therefore likely that in the EPGGT,  $q_c \sim 60 \pm 10 \text{ mW m}^{-2}$  at the time of major Mid- to Late Archaean tectonothermal activity.

However, the real importance of such high Archaean  $q_c$  values lies in the fact that parameters such as geotherm curvature and Moho temperature ( $T_{\text{Moho}}$ ) are remarkably sensitive to the *depth distribution* of the HPEs (see also Sandiford and Hand, 1998; Sandiford and McLaren, 2002; Sandiford et al., 2002). For example, the eruption or emplacement of a 5 km thick greenstone sequence atop a granitic crust similar to EPGGT in the Late Archaean ( $k = 3 \text{ W m}^{-1} \text{ } ^\circ\text{C}^{-1}$ ,  $q_c = 60 \text{ mW m}^{-2}$ ) gives  $\Delta T_{\text{Moho}} = +100^\circ\text{C}$ , following conductive re-equilibration of the geotherm. This temperature increase is purely due to the burial of crust-hosted HPEs, and is entirely independent of heating associated with deepening of the Moho relative to the Earth's surface (which is neglected here). Considering  $T_{\text{Moho}}$  as a proxy for the strength of the upper lithosphere in this scenario (see Sonder and England, 1986), conductive re-equilibration of Archaean geotherms following HPE burial has significant potential for thermal weakening of the lower crust, and provides a possible trigger for large-scale tectonic processes such as dome-and-keel formation (e.g. Marshak et al., 1997; Sandiford et al., in press).

Based on these ideas, we surmise that both the abundance of HPEs and their depth distribution are crucial factors in the preservation of many Archaean crustal segments, especially those that display little evidence of subsequent tectonic reworking. Geological processes that act to concentrate HPEs at shallow crustal levels play a critical role in the long-term cooling (and strengthening) of the uppermost lithosphere,

and the vertical ascent of large, HPE-rich granitoid complexes into overlying greenstone sequences during dome-and-keel formation represents an extremely efficient method by which such HPE “shallowing” may be accomplished (see also Sandiford et al., 2002, in press). It is thus possible that even relatively high- $q_c$  crust (such as the EPGGT) may be highly resistant to subsequent reactivation if vertical HPE differentiation is efficient enough, and such a mechanism might explain why cratons with well-developed dome-and-keel structure (e.g. Pilbara, Kaapvaal) generally contain a higher proportion of Archaean supracrustal rocks that have undergone relatively little pervasive deformation or high-grade metamorphism (e.g. Van Kranendonk, 2000; Hofmann et al., 2001; Thurston, 2002; Sandiford et al., in press).

## 10. Summary and conclusions

Determining the heat production budget of Archaean crust is critical to the understanding of factors influencing the thermal and mechanical evolution and stabilisation of Precambrian lithosphere, and obtaining accurate estimates of HPE concentrations in major rock units within the uppermost crust is an important part of the process. In the EPGGT, the availability of high-quality radiometric data and extensive geochemistry provided a unique opportunity to assess the usefulness of airborne gamma-ray spectrometry to the quantitative estimation of area-averaged surface heat production in a well-exposed terrane, and our major findings are:

- (1) Overall, spatial and attribute accuracy of HPE values derived from the calibrated radiometric dataset is high. Sample-by-sample comparison of the radiometric data with ground control provided by bedrock geochemistry showed that first-order agreement is good for all HPEs (except U in mafic rocks), with 20–40% of all  $\xi$  values lying in the range 0.95–1.05.
- (2) For the most part, high frequencies in the  $\xi$  spectra away from  $\xi \sim 1$  reflect reasonable and predictable geochemical behaviour of HPEs in surface environments. Physical and/or chemical homogenisation of soils ( $\xi > 1$  in felsic rocks,  $\xi < 1$  in mafic rocks for all HPEs) is inevitable

when the geochemistry of the underlying bedrock is strongly bimodal. Widespread but variable depletion of K in the surface layer ( $\xi_K > 1$ ) is due to the mobility of K during chemical weathering, and its susceptibility to redistribution at all scales. Outliers in the  $\xi_U$  spectrum (mostly  $\xi_U < 1$ ) primarily reflect the sensitivity of gamma-ray data to surface-layer disequilibrium in the  $^{238}\text{U}$  decay chain, but may also point to systematic problems in the determination of bedrock U for some of the geochemical data, possibly stemming from inadequate accuracy and/or precision of the analytical technique(s) employed.

- (3) The  $\xi$  data are valuable as a first-order indicator of the correction needed to minimise the effect of small-scale HPE modification processes in the surface layer, thereby enhancing agreement between the radiometric and geochemical data at sub-unit scale in the EPGGT granitoid complexes. Area-averaged heat production estimates derived from the  $\xi$ -multiplied radiometric data are in excellent agreement with the mean value determined from the available geochemistry (present-day  $H = 1.5\text{--}2.5 \mu\text{W m}^{-3}$  for most of the pre-2.9 Ga granitic sub-units in the EPGGT, rising to  $H = 4.0\text{--}6.5 \mu\text{W m}^{-3}$  for late-stage, low-volume plutons in the Mount Edgar, Shaw and Yule granitoid complexes). In addition, the large sample space in the gamma-ray data relative to the geochemical dataset ensures both a truer representation of each sub-unit component with respect to the area-averaged statistics, and a smaller standard deviation about the mean value, that more accurately reflects true geochemical variation at pluton-scale.
- (4) Using the  $\xi$ -multiplied HPE data in simple 2D and 3D models of the EPGGT lithosphere yielded a thermal configuration consistent with independent constraints imposed by surface heat flow measurements. Our models suggest that the HPE-related contribution to the surface heat flow  $q_c \sim 30 \pm 5 \text{ mW m}^{-2}$ , a range of values similar to that deduced for many Proterozoic terrains worldwide. This result implies that the abundance of crust-hosted HPEs alone does not always exert primary control on the preservation of ancient crust (cf. Morgan, 1985). Rather, in view of the sensitivity of thermal regimes in the

upper lithosphere to both the abundance *and* the depth distribution of HPEs (see also Sandiford and McLaren, 2002 and references therein), we consider it likely that Precambrian terrains characterised by the efficient concentration of HPEs in the upper crust exemplify thermally and mechanically stable configurations that are resistant to subsequent reworking. The spectacular, large-scale development of dome-and-keel architecture in the EPGGT is an excellent example of such a differentiation process (Sandiford et al., *in press*).

### Acknowledgements

The authors would like to thank David Champion (Geoscience Australia) and Hugh Smithies (Geological Survey of Western Australia) for their assistance with the OZCHEM database, and Dallas Abbott and Peter Wellman for thoughtful and constructive reviews. Brian Minty and Richard Blewett publish with the permission of the Executive Director, Geoscience Australia. This research was partially funded by Australian Research Council Discovery-Project grant DP0208176, awarded to Simon Bodorkos.

### References

- Arndt, N.T., Nelson, D.R., Compston, W., Trendall, A.F., Thorne, A.M., 1991. The age of the Fortescue Group, Hamersley Basin, Western Australia, from ion microprobe zircon U-Pb results. *Aust. J. Earth Sci.* 38, 261–281.
- Artemieva, I.M., Mooney, W.D., 2001. Thermal thickness and evolution of Precambrian lithosphere: a global study. *J. Geophys. Res.* 106, 16387–16414.
- Ashwal, L.D., Morgan, P., Kelley, S.A., Percival, J.A., 1987. Heat production in an Archean crustal profile and implications for heat flow and mobilization of heat-producing elements. *Earth Planet. Sci. Lett.* 85, 439–450.
- Bagas, L., Van Kranendonk, M.J., Pawley, M., 2002. Split Rock W.A. 1:100,000 Geological Sheet 2854. Geological Survey of Western Australia, Perth.
- Ballard, S., Pollack, H.N., 1987. Diversion of heat by Archean cratons: a model for southern Africa. *Earth Planet. Sci. Lett.* 85, 253–264.
- Barley, M.E., Pickard, A.L., 1999. An extensive, crustally-derived, 3325 to 3310 Ma silicic volcanoplutonic suite in the eastern Pilbara Craton: evidence from the Kelly Belt, McPhee Dome and Corunna Downs Batholith. *Precambrian Res.* 96, 41–62.

- Beardsmore, G.R., Cull, J.P., 2001. *Crustal Heat Flow: A Guide to Measurement and Modelling*. Cambridge University Press, Cambridge, 324 pp.
- Bickle, M.J., Bettenay, L.F., Chapman, H.J., Groves, D.I., McNaughton, N.J., Campbell, I.H., de Laeter, J.R., 1993. Origin of the 3500–3300 Ma calc-alkaline rocks in the Pilbara Archæan: isotopic and geochemical constraints from the Shaw Batholith. *Precambrian Res.* 60, 117–149.
- Bierwirth, P.N., 1996. Investigation of airborne gamma-ray images as a rapid mapping tool for soil and land degradation—Wagga Wagga, NSW. AGSO Record 1996/22. Australian Geological Survey Organisation, Canberra.
- Blewett, R.S., 2002. Archæan tectonic processes: a case for horizontal shortening in the North Pilbara Granite–Greenstone Terrane, Western Australia. *Precambrian Res.* 113, 87–120.
- Blewett, R.S., Wellman, P., Ratajkoski, M., Huston, D.L., 2000. Atlas of North Pilbara geology and geophysics: 1:1.5 million scale. AGSO Record 2000/4. Australian Geological Survey Organisation, Canberra.
- Boyd, F.R., Gurney, J.J., Richardson, S.H., 1985. Evidence for a 150–200 km thick Archæan lithosphere from diamond inclusion thermobarometry. *Nature* 315, 387–389.
- Brace, W.F., Kohlstedt, D.L., 1980. Limits on lithospheric strength imposed by laboratory experiments. *J. Geophys. Res.* 85, 6248–6252.
- Buick, R., Thornett, J.R., McNaughton, N.J., Smith, J.B., Barley, M.E., Savage, M., 1995. Record of emergent continental crust ~3.5 billion years ago in the Pilbara craton of Australia. *Nature* 375, 574–577.
- Champion, D.C., Smithies, R.H., 2000. The geochemistry of the Yule Granitoid Complex, East Pilbara Granite–Greenstone Terrane: evidence for early felsic crust. In: Geological Survey of Western Australia Annual Review 1999/2000, pp. 42–48.
- Collins, W.J., 1989. Polydiapirism of the Archæan Mount Edgar Batholith, Pilbara Block, Western Australia. *Precambrian Res.* 43, 41–62.
- Collins, W.J., 1993. Melting of Archæan sialic crust under high aH<sub>2</sub>O conditions: genesis of 3300 Ma Na-rich granitoids in the Mount Edgar Batholith, Pilbara Block, Western Australia. *Precambrian Res.* 60, 151–174.
- Cull, J.P., 1982. An appraisal of Australian heat-flow data. *BMR J. Aust. Geol. Geophys.* 7, 11–21.
- Cull, J.P., 1991. Heat flow and regional geophysics in Australia. In: Cermak, V., Rybach, L. (Eds.), *Terrestrial Heat Flow and the Lithosphere Structure*. Springer-Verlag, Berlin, pp. 486–500.
- Dickson, B.L., 1995. Uranium-series disequilibrium in Australian soils and its effect on aerial gamma-ray surveys. *J. Geochem. Explor.* 54, 177–186.
- Dickson, B.L., Scott, K.M., 1997. Interpretation of aerial gamma-ray surveys—adding the geochemical factors. *AGSO J. Aust. Geol. Geophys.* 17 (2), 187–200.
- Drummond, B.J., 1983. Detailed seismic velocity/depth models of the upper lithosphere of the Pilbara Craton, northwest Australia. *BMR J. Aust. Geol. Geophys.* 8, 35–51.
- Drummond, B.J., 1988. A review of crust/upper mantle structure in the Precambrian areas of Australia and implications for Precambrian crustal evolution. *Precambrian Res.* 40/41, 101–116.
- Fountain, D.M., Salisbury, M.H., Furlong, K.P., 1987. Heat production and thermal conductivity of rocks from the Pikwitonei–Sachigo continental cross section, central Manitoba: implications for the thermal structure of Archæan crust. *Can. J. Earth Sci.* 24, 1583–1594.
- Glikson, A.Y., 1998. Landsat-5-Thematic Mapper spectral—lithological correlations, northern Pilbara Craton, Western Australia. AGSO Record 1998/22. Australian Geological Survey Organisation, Canberra.
- Grand, S.P., Helmberger, D.V., 1984. Upper mantle shear structure of North America. *Geophys. J. R. Astronom. Soc.* 76, 399–438.
- Griffin, T.J., 1990. North Pilbara Granite–Greenstone Terrane. In: *Geology and Mineral Resources of Western Australia*. Geological Survey of Western Australia Memoir 3, pp. 128–158.
- Gruau, G., Jahn, B.-M., Glikson, A.Y., Davy, R., Hickman, A.H., Chauvel, C., 1987. Age of the Archæan Talga Talga Subgroup, Pilbara Block, Western Australia, and early evolution of the mantle: new Sm–Nd isotopic evidence. *Earth Planet. Sci. Lett.* 85, 105–116.
- Haenel, R., Rybach, L., Stegena, L., 1988. *Handbook of Terrestrial Heat-Flow Density Determination, with Guidelines and Recommendations of the International Heat Flow Commission*. Kluwer Academic Publishers, Dordrecht, 486 pp.
- Hickman, A.H., 1983. *Geology of the Pilbara Block and its environs*. GSWA Bull. 127. Geological Survey of Western Australia, Perth.
- Hickman, A.H., Lipple, S.L., 1978. Marble Bar W.A. 1:250,000 Geological Sheet SF 50-8. Geological Survey of Western Australia, Perth.
- Hofmann, A., Dirks, P.H.G.M., Jelsma, H.A., 2001. Horizontal tectonic deformation geometries in a Late Archæan sedimentary sequence, Belingwe greenstone belt, Zimbabwe. *Tectonics* 20, 909–932.
- Ivanovich, M., Harmon, R.S. (Eds.), 1992. *Uranium Series Disequilibrium: Applications to Earth, Marine and Environmental Sciences*. Clarendon Press, Oxford, 910 pp.
- Jaupart, C., Mareschal, J.C., 1999. The thermal structure and thickness of continental roots. *Lithos* 48, 93–114.
- Jordan, T.H., 1978. Composition and development of the continental tectosphere. *Nature* 274, 544–548.
- Jordan, T.H., 1988. Structure and formation of the continental tectosphere. In: Menzies, M.A., Cox, K.G. (Eds.), *Oceanic and Continental Lithosphere: Similarities and Differences*. J. Petrol. (Special Lithosphere Issue), pp. 11–37. Oxford University Press, London.
- Kukkonen, I.T., Lahtinen, R., 2001. Variation of radiogenic heat production rate in 2.8–1.8 Ga old rocks in the central Fennoscandian Shield. *Phys. Earth Planet. Interiors* 126, 279–294.
- Lenardic, A., 1997. On the heat flow variation from Archæan cratons to Proterozoic mobile belts. *J. Geophys. Res.* 102, 709–721.
- Marshak, S., Tinkham, D., Alkmim, F., Brueckner, H., Bornhost, T., 1997. Dome-and-keel provinces formed during Palaeo-proterozoic orogenic collapse—core complexes, diapirs, or



- neither?: Examples from the Quadrilatero Ferrifero and the Penokean Orogen. *Geology* 25, 415–418.
- McLennan, S.M., Taylor, S.R., 1996. Heat flow and the chemical composition of continental crust. *J. Geol.* 104, 369–377.
- Minty, B.R.S., 1997. Fundamentals of airborne gamma-ray spectrometry. *AGSO J. Aust. Geol. Geophys.* 17 (2), 39–50.
- Minty, B.R.S., Luyendyk, A.P.J., Brodie, R.C., 1997. Calibration and data processing for airborne gamma-ray spectrometry. *AGSO J. Aust. Geol. Geophys.* 17 (2), 51–62.
- Morgan, P., 1985. Crustal radiogenic heat production and the selective survival of ancient continental crust. *J. Geophys. Res.* 90, C561–C570.
- Nelson, D.R., 1998. Compilation of SHRIMP U-Pb zircon geochronology data, 1997. GSWA Record 1998/2. Geological Survey of Western Australia, Perth.
- Nelson, D.R., 2000. Compilation of geochronology data, 1999. GSWA Record 2000/2. Geological Survey of Western Australia, Perth.
- Nelson, D.R., 2001. Compilation of geochronology data, 2000. GSWA Record 2001/2. Geological Survey of Western Australia, Perth.
- Nicolaysen, L.O., Hart, R.J., Gale, N.H., 1981. The Vredefort radioelement profile extended to supracrustal strata at Carletonville, with implications for continental heat flow. *J. Geophys. Res.* 86, 10653–10661.
- Nyblade, A.A., Pollack, H.N., 1993. A global analysis of heat flow from Precambrian terrains: implications for the thermal structure of Archean and Proterozoic lithosphere. *J. Geophys. Res.* 98, 12207–12218.
- Nyblade, A.A., Pollack, H.N., Jones, D.L., Podmore, F., Mushayandebvu, M., 1990. Terrestrial heat flow in east and southern Africa. *J. Geophys. Res.* 95, 17371–17384.
- Polet, J., Anderson, D.L., 1995. Depth extent of cratons as inferred from tomographic studies. *Geology* 23, 205–208.
- Pollack, H.N., 1986. Cratonization and thermal evolution of the mantle. *Earth Planet. Sci. Lett.* 80, 175–182.
- Pollack, H.N., Hurter, S., Johnson, J.R., 1993. Heat flow from the Earth's interior: analysis of the global data set. *Rev. Geophys.* 31, 267–280.
- Richardson, L.M., 1997. Marble Bar (Marble Bar, western Port Hedland, eastern Roebourne and northeastern Pyramid 1:250,000 sheet areas) airborne geophysical survey, 1996—operations report. AGSO Record 1997/63. Australian Geological Survey Organisation, Canberra.
- Ritsema, J., van Heijst, H., 2000. New seismic model of the upper mantle beneath Africa. *Geology* 28, 63–66.
- Rudnick, R.L., Fountain, D.M., 1995. Nature and composition of the continental crust: a lower crustal perspective. *Rev. Geophys.* 33, 267–309.
- Rudnick, R.L., McDonough, W.F., O'Connell, R.J., 1998. Thermal structure, composition and thickness of continental lithosphere. *Chem. Geol.* 145, 395–411.
- Russell, J.K., Dipple, G.M., Kopylova, M.G., 2001. Heat production and heat flow in the mantle lithosphere, Slave craton, Canada. *Phys. Earth Planet. Interiors* 123, 27–44.
- Sandiford, M., Hand, M., 1998. Australian Proterozoic high-temperature, low-pressure metamorphism in the conductive limit. In: Treloar, P.J., O'Brien, P.J. (Eds.), *What Drives Metamorphism and Metamorphic Reactions?* Geological Society of London Special Publication 138, pp. 109–120.
- Sandiford, M., McLaren, S., 2002. Tectonic feedback and the ordering of heat producing elements within the continental lithosphere. *Earth Planet. Sci. Lett.* 204, 133–150.
- Sandiford, M., Hand, M., McLaren, S., 2001. Tectonic feedback, intraplate orogeny and the geochemical structure of the crust: a central Australian perspective. In: Miller, J., Buick, I.S., Hand, M., Holdsworth, R.E. (Eds.), *Continental Reactivation and Reworking*. Geological Society of London Special Publication 184, pp. 195–218.
- Sandiford, M., McLaren, S., Neumann, N., 2002. Long-term thermal consequences of the redistribution of heat-producing elements associated with large-scale granitic complexes. *J. Metamorph. Geol.* 20, 87–98.
- Sandiford, M., Van Kranendonk, M.J., Bodorkos, S., in press. Conductive incubation and the origin of dome-and-keel structure in Archean granite–greenstone terrains: a model based on the eastern Pilbara Craton, Western Australia. *Tectonics*.
- Simons, F.J., Zielhuis, A., van der Hilst, R.D., 1999. The deep structure of the Australian continent from surface wave tomography. *Lithos* 48, 17–43.
- Sonder, L.J., England, P., 1986. Vertical averages of rheology of the continental lithosphere: relation to thin sheet parameters. *Earth Planet. Sci. Lett.* 77, 81–90.
- Taylor, S.R., McLennan, S.M., 1995. The geochemical evolution of the continental crust. *Rev. Geophys.* 33, 241–265.
- Thorne, A.M., Trendall, A.F., 2001. The geology of the Fortescue Group, Hamersley Basin, Western Australia. GSWA Bull. 144. Geological Survey of Western Australia, Perth.
- Thurston, P.C., 2002. Autochthonous development of Superior Province greenstone belts? *Precambrian Res.* 105, 11–36.
- Turcotte, D.L., Schubert, G., 1982. *Geodynamics: Applications of Continuum Physics to Geological Problems*. John Wiley & Sons, New York, 450 pp.
- Van Kranendonk, M.J., 2000. Geology of the North Shaw 1:100,000 sheet, Western Australia. 1:100,000 Geological Series Explanatory Notes. Geological Survey of Western Australia, Perth.
- Van Kranendonk, M.J., 2003. Stratigraphic and tectonic significance of eight local unconformities in the Fortescue Group, Pear Creek Centrocline, Pilbara Craton, Western Australia. In: *Geological Survey of Western Australia Annual Review 2001/2002*, pp. 70–79.
- Van Kranendonk, M.J., Collins, W.J., 1998. Timing and tectonic significance of Late Archean, sinistral strike-slip deformation in the Central Pilbara Structural Corridor, Pilbara Craton, Western Australia. *Precambrian Res.* 88, 207–232.
- Van Kranendonk, M.J., Hickman, A.H., Williams, I.R., Nijman, W., 2001. Archean geology of the East Pilbara Granite–Greenstone Terrane, Western Australia—a field guide. GSWA Record 2001/9. Geological Survey of Western Australia, Perth.
- Van Kranendonk, M.J., Hickman, A.H., Smithies, R.H., Nelson, D.R., Pike, G., 2002. Geology and tectonic evolution of the Archean North Pilbara Terrain, Pilbara Craton, Western Australia. *Econ. Geol.* 97, 695–732.

- Vigneresse, J.L., Cuney, M., 1991. Are granites representative of heat flow provinces? In: Cermak, V., Rybach, L. (Eds.), *Terrestrial Heat Flow and the Lithosphere Structure*. Springer-Verlag, Berlin, pp. 86–110.
- Weaver, B.L., Tarney, J., 1984. Empirical approach to estimating the composition of the continental crust. *Nature* 310, 575–577.
- Wellman, P., 1998a. Gamma-ray spectrometric data: modelling to map primary lithology and later chemical mobilisation. *AGSO Res. Newslett.* 28, 18–19.
- Wellman, P., 1998b. Mapping of a granite batholith using geological and remotely sensed data: the Mount Edgar Batholith, Pilbara Craton. *Explor. Geophys.* 29, 643–648.
- Wellman, P., 1999. Interpretation of regional geophysics of the Pilbara Craton, northwest Australia. *AGSO Record* 1999/4. Australian Geological Survey Organisation, Canberra.
- Wellman, P., 2000. Upper crust of the Pilbara Craton, Australia: 3D geometry of a granite/greenstone terrain. *Precambrian Res.* 104, 175–186.
- Wilford, J.R., Bierwirth, P.N., Craig, M.A., 1997. Application of airborne gamma-ray spectrometry in soil/regolith mapping and applied geomorphology. *AGSO J. Aust. Geol. Geophys.* 17 (2), 201–216.
- Wingate, M.T.D., 1999. Ion microprobe baddeleyite and zircon ages for Late Archaean mafic dykes of the Pilbara Craton, Western Australia. *Aust. J. Earth Sci.* 46, 493–500.